



OPEN

DATA DESCRIPTOR

Dynamical reconstruction of Southern Ocean and Antarctic climate variability since 1700

Quentin Dalaiden^{1,2}✉, Hugues Goosse², Paul R. Holland³ & Antoine Barthelemy²

Understanding long-term climate variability in the high latitudes of the Southern Hemisphere is critical due to the key role of the Southern Ocean in the global climate system. However, sparse observations (in space and time) coupled with strong internal variability limit our ability to interpret the origin of recent changes, and their longer-term context. Here we present a dynamically consistent reconstruction of the Antarctic atmosphere and Southern Ocean from 1700 to 2023. We first use data assimilation (DA)-based Antarctic atmospheric reanalyses that combine instrumental observations (1958–2023) and paleoclimate proxies (1700–2000) with Earth System Models to reconstruct key surface climate fields. We then drive a global ocean–sea-ice model with this atmospheric reanalysis to simulate historical ocean conditions, including temperature, salinity, currents, and sea-ice-related variables at 1° resolution. This reconstruction provides the first long-term physically consistent dataset of Antarctic atmosphere–ocean variability, suitable for studying low-frequency climate variability, evaluating climate models, and potentially driving regional atmospheric and ocean models as well as ice sheet models.

Background & Summary

The high-latitude regions of the Southern Hemisphere have undergone substantial climate changes in recent decades¹. West Antarctica, in particular, has experienced one of the most pronounced warming trends globally since 1958². Meanwhile, Antarctic sea-ice extent showed a surprising positive trend from 1979 to 2014, before dropping to record-low levels in subsequent years^{3,4}. These surface changes are tightly coupled with changes in atmospheric circulation, including the intensification and poleward shift of westerly winds and modified meridional heat and moisture transport – key drivers of regional climate variability^{5–9}. At the same time, the Southern Ocean has warmed since the mid-20th century^{10,11}, contributing to broader changes in the coupled ocean–ice–atmosphere system¹². These climate changes have had major direct and indirect implications for the Antarctic Ice Sheet (AIS). While snow accumulation generally increased over the 20th century¹³ – albeit strong spatial variability has been noticed^{13–18} –, observed basal melt rates of ice shelves (floating extensions of grounded Antarctic glaciers) since the 1990s have exceeded the historical rate at which the glaciers would be in balance. In particular, there are evidence that glaciers located in the Amundsen Sea are experiencing high melt rates since the 1970s^{19,20}, and possibly as early as the 1940s²¹. This melting is primarily driven by the intrusion of relatively warm ocean waters into ice shelf cavities^{22–25}, which undermines ice shelf stability and contributes to AIS mass loss. As these losses overall outpaced surface mass gains from snowfall, the net effect is a growing Antarctic contribution to global sea-level rise²⁵. This highlights the urgent need to better understand historical climate variability in the high latitudes of the Southern Hemisphere, along with its atmospheric and oceanic drivers as well as their interactions.

The climate of the high-latitude Southern Hemisphere is characterized by strong natural variability²⁶. However, observational records in these regions are limited in time, making it difficult to place recent changes in a longer-term context. Most studies of surface climate trends rely on satellite observations, which only became widely available in 1979. For the Southern Ocean, reliable observational records are even more reduced, with data primarily starting in the 1990s for areas closed to the Antarctic coast¹¹. This limited temporal coverage is especially problematic given the pronounced variability in these regions, which complicates the interpretation of

¹Nansen Environmental and Remote Sensing Center and Bjerknes Center for Climate Research, Bergen, Norway.

²Earth and Life Institute, Université catholique de Louvain, Louvain-la-Neuve, Belgium. ³British Antarctic Survey, Cambridge, CB3 0ET, UK. ✉e-mail: quentin.dalaiden@nersc.no

ongoing changes. It also poses challenges for evaluating climate models, which often display substantial biases in Antarctic regions^{27,28}. As a result, it remains difficult to determine whether discrepancies between model results and observations arise from model deficiencies or from internal climate variability. To address this gap, recent efforts have developed historical reconstructions of the Antarctic surface climate over the past few centuries. These reconstructions combine the physics-based framework of Earth System Models (ESMs) with indirect climate records (i.e., climate proxies)^{29–31}. However, such reconstructions have mainly focused on atmospheric and sea-ice variables, particularly temperature, precipitation, and wind. In contrast, the ocean remains comparatively understudied. Although past efforts have used sediment cores to infer surface ocean variability³², comprehensive reconstructions of historical ocean conditions are still lacking.

Longer time-series of historical changes of both the atmosphere and ocean are therefore essential for contextualizing the current changes and for understanding the physical mechanisms behind this climate variability, in particular at the low-frequency variability, which is largely unknown. This limitation is particularly critical for future projections of global sea level, as the largest uncertainties arise from the contribution of the Antarctic Ice Sheet^{33,34}. Since these uncertainties are primarily linked to the complex interactions between the ocean and ice shelves, without sufficient information on past climate variability in the Southern Ocean, accurately initializing ice sheet models remains highly challenging and poorly constrained, significantly contributing to the large uncertainties in future sea-level projections³⁵. Regarding the past variability, historical simulations (1850–2014) from the Coupled Model Intercomparison Project Phase 6 (CMIP6) have been recently used to investigate the mass balance variability of the AIS³⁶. However, as noted by the authors, these CMIP6 simulations are not directly constrained by observations (only external forcing), meaning that the phase of natural variability might be strongly different from reality. Additionally, several studies have shown that these CMIP6 historical simulations likely underestimate the amplitude of internal variability^{37,38}. These limitations pose challenges for directly comparing simulations with observations and for attributing observed changes.

In this work, we employ both Data Assimilation (DA) and a global ocean–sea-ice model to provide a consistent reconstruction of past climate variations at the high latitudes of the Southern Hemisphere from 1700 to 2023. DA-based approaches have the advantage of utilizing a Bayesian framework to update the initial state of the entire system by incorporating information from available observations. Although DA-based methods have been increasingly used to reconstruct historical climate variability in recent years^{39–41}, no comprehensive dataset specifically focused on Antarctica is currently available. DA-based methods enable the reconstruction of specific variables that are assimilated, such as temperature and pressure, as well as non-assimilated variables like sea-ice cover and winds, by utilizing the dynamical relationships between the reconstructed variables. Specifically, DA-based techniques integrate observational data with climate models to propagate local information across space and between different variables, using the modeled covariance from the climate model. This ensures dynamical consistency among all reconstructed variables.

As a first step, we focus on reconstructing atmospheric variables, by providing a long-term atmospheric reanalysis over Antarctica. To this end, we extend the satellite observation period to 1958 (i.e., beginning of instrumental observations in Antarctica⁴²) by using the recent atmospheric reanalysis of Goosse *et al.*⁴³, which employed a DA-based method that combines 10 Large Ensembles (LEs) – performed with 10 different Earth System Models (ESMs) – and 27 long observational time series of near-surface air temperature and atmospheric surface pressure from the mid-latitude region and Antarctica. This reconstruction is referred to as station-based reanalysis. This method, using instrumental observations, provides historical data on key atmospheric variables (i.e., near-surface air temperature, sea-level pressure, precipitation, winds, and heat fluxes), as well as sea surface conditions (sea-ice cover and sea surface temperature) around Antarctica from 1958 to 2023, with annual temporal resolution and 1-degree spatial resolution. Before 1958, we need to rely on indirect climate records, in particular paleoclimate records. Therefore, we utilize the reconstruction published by Dalaiden, Rezsóhazy *et al.*³¹, which follows the same methodology as the station-based reanalysis but incorporates more than 100 paleoclimate proxy records from the mid-latitude and Antarctic regions. This reconstruction, referred to as paleo-based reanalysis, spans the period from 1700 to 2000, with annual resolution and 2-degree spatial resolution. In contrast to the station-based reanalysis, the paleo-based reanalysis is based on solely one model, the isotope-enabled Community Earth System Model version 1 (iCESM1)^{44,45}. These two reanalyses only cover the Southern Ocean.

In the second step, we use an ocean–sea-ice model forced by our atmospheric reconstructions to provide historical changes for the ocean from 1700–2023. Forcing an ocean model is one approach to reconstruct the historical variability of the ocean in response to atmospheric changes⁴⁶. Specifically, we employ a 1-degree global configuration of the Nucleus for European Modelling of the Ocean (NEMO) with the largest ice shelf cavities open⁴⁷. Since the paleo-based atmospheric reanalysis does not span the period after 2000, the atmospheric forcing is constructed by combining the station-based reanalysis and paleo-based reanalysis. Besides, these reanalyses only cover the high latitudes of the Southern Hemisphere, we therefore combine them with a global atmospheric reconstruction covering the past 600 years⁴¹ to obtain a global atmospheric forcing. As NEMO requires high-frequency input for atmospheric forcing, we develop an algorithm to generate 6-hourly forcing by combining the annual reconstructions with state-of-the-art atmospheric reanalysis.

The atmospheric reanalysis and ocean simulation spanning 1700–2023 provide, for the first time, a dynamically consistent reconstruction of historical climate changes over Antarctica, encompassing both the atmosphere and the ocean. All standard three-dimensional ocean variables are estimated, including temperature, salinity, sea-ice-related variables, and ocean velocities. By including dynamical variables, such as changes in atmospheric and oceanic circulation, this dataset offers a unique opportunity to understand the underlying mechanisms of the long-term climate variability in the high latitudes of the Southern Hemisphere. We aim to provide a dynamically coherent atmosphere–ocean reconstruction over the past centuries to support a range of applications. This dataset enables the study of low-frequency climate variability over Antarctica – a key component of decadal and

multi-decadal variability with significant implications but under-investigated due to the shortness of observational time-series. This dataset can be thus used to assess variability in ESMs – which is strongly underestimated when comparing to observations³⁸. Furthermore, our longer historical sea-surface conditions can be used to force atmospheric models, including polar-oriented regional atmospheric models, to simulate surface climate over the Antarctic Ice Sheet and assess long-term changes, placing satellite-era observations in a broader temporal context. Ultimately, the main purpose of this dataset is to drive ice sheet models. Forcing ice sheet models with this reconstruction offers, most probably, a more realistic representation of the role of natural variability in Antarctic mass balance than current simulations based on CMIP historical simulations³⁶.

Method

Atmospheric reconstruction. *Offline data assimilation.* To reconstruct the atmospheric variability and surface conditions over the past decades and centuries, we employ a Data Assimilation (DA) method, which optimally fuses the information from observations and climate models. More specifically, data assimilation starts with an initial state of the system (i.e., the climate state; \mathbf{x}^p) provided by the climate model simulations, called the prior. Afterwards, the prior is updated according to the available observations (\mathbf{y}), which gives the final state of the climate system, the posterior. In this study, the used data assimilation method is based on a particle filter⁴⁸, following the implementation of Dubinkina *et al.*⁴⁹. This method has been successfully applied in recent years to reconstruct the climate variability during the past centuries^{29,31,50,51}. DA is based on the Bayes theorem:

$$p(\mathbf{x}^p|\mathbf{y}) = \frac{p(\mathbf{y}|\mathbf{x}^p)p(\mathbf{x}^p)}{p(\mathbf{y})} \quad (1)$$

In this equation, $p(\mathbf{x}^p|\mathbf{y})$ is the posterior probability distribution function (pdf). $p(\mathbf{x}^p)$ and $p(\mathbf{y})$ correspond to the prior and the distribution of observations, respectively. $p(\mathbf{y}|\mathbf{x}^p)$ represents the conditional probability of observations given the prior (i.e., the likelihood). This term can be further written as follows:

$$p(\mathbf{y}|\mathbf{x}^p) = K^{-1} \exp\left[-\frac{1}{2}(\mathbf{y} - H(\mathbf{x}^p))^T R^{-1}(\mathbf{y} - H(\mathbf{x}^p))\right] \quad (2)$$

where K^{-1} is a normalization constant (as such that the cumulative distribution function is unity), H corresponds to the operator that maps the prior to the observational phase space (see the section related to the Forward operator for details). R represents the error covariance matrix induced by the model-data comparison and is assumed here to be diagonal (the errors are independent of each other).

The approach outlined by van Leeuwen⁴⁸ involves approximating the prior through a discrete distribution built from independent model states known as particles. This methodology, known as particle filtering, requires more particles for complex systems than simpler ones, so more particles are required when assimilating a larger amount of observations. Unlike the common sequential DA method, which propagates information forward in time (referred to as online data assimilation⁵²), we employ the offline version of the particle filter. The offline DA method, also known as the no-cycling method, relies on a fixed prior for every timestep of the DA. It means that the state at time $t-1$ does not influence the state at time t . The temporal variability of the posterior therefore only comes from the variability within the assimilated observations. Offline methods have a large advantage since they allow using existing model simulations. Applying online DA methods using CMIP-class Earth System Models directly to reconstruct the climate over the past centuries has not been achieved yet because of the enormous computational expense this would require. Since we aim to reconstruct the hydroclimate at the interannual variability (the timestep of the assimilation is one year), offline methods are appropriate. This is supported by the study of Matsikaris *et al.*⁵³, which demonstrated that online methods do not outperform offline methods in reconstructing hydroclimate, which is predominantly influenced by atmospheric processes, at this timescale. In this context, the prior can be written as follows:

$$p(\mathbf{x}^p) = \frac{1}{N} \sum_{i=1}^N \delta(\mathbf{x}^p - \mathbf{x}_i^p) \quad (3)$$

N is the number of particles while δ corresponds to a kernel density. Since we have no information about the likelihood of each particle, each particle is an equal weight when building the prior. By combining Eqs. (1) and (3), the posterior can be re-written as:

$$p(\mathbf{x}^p|\mathbf{y}) = \frac{1}{N} \sum_{i=1}^N w_i \delta(\mathbf{x}^p - \mathbf{x}_i^p) \quad (4)$$

with,

$$w_i = \frac{p(\mathbf{y}|\mathbf{x}_i^p)}{\sum_{j=1}^N p(\mathbf{y}|\mathbf{x}_j^p)} \quad (5)$$

We can insert Eq. (2) into Eq. (5) for calculating the weight of each particle depending on its likelihood relative to observations, w_i :

ESM	Spanned period	Size of the ensemble	Reference
station-based reanalysis			
ACCESS-ESM1-5	1950 – 2100	40	Rashid <i>et al.</i> ¹¹²
CanESM2	1950 – 2023	50	Kirchmeier-Young <i>et al.</i> ¹¹³
CanESM5	1850 – 2014	40	Swart <i>et al.</i> ¹¹⁴
CESM1	850 – 2005	12	Otto-Bliesner <i>et al.</i> ¹¹⁵
CESM2	1850 – 2023	100	Rodgers <i>et al.</i> ¹¹⁶
CNRM-CM6-1	1850 – 2014	19	Voldoire <i>et al.</i> ¹¹⁷
IPSL-CM6A-LR	1850 – 2014	33	Boucher <i>et al.</i> ¹¹⁸
MPI-ESM	1850 – 2023	100	Maher <i>et al.</i> ¹¹⁹
NorCPM1	1850 – 2014	30	Bethke <i>et al.</i> ¹²⁰
UKESM1-0-LL	1850 – 2014	14	Sellar <i>et al.</i> ¹²¹
paleo-based reanalysis			
iCESM1	850 – 2005	3	Brady <i>et al.</i> ⁴⁴ ; Stevenson <i>et al.</i> ⁴⁵

Table 1. Details of the Large Ensembles used to construct the prior for both the station- and paleo-based atmospheric reanalyses, including information about the Earth System Model, the period covered by the ensemble, the number of ensemble members, and the reference.

$$w_i = \frac{\exp\left[-\frac{1}{2}(\mathbf{y} - H(\mathbf{x}_i^p))^T R^{-1}(\mathbf{y} - H(\mathbf{x}_i^p))\right]}{\sum_{j=1}^N \exp\left[-\frac{1}{2}(\mathbf{y} - H(\mathbf{x}_j^p))^T R^{-1}(\mathbf{y} - H(\mathbf{x}_j^p))\right]} \quad (6)$$

Throughout the study, the mean of the posterior is considered as the reconstruction, which is calculated as the weighted mean of all the particles:

$$\overline{p(\mathbf{x}^p|\mathbf{y})} = \sum_{j=1}^N w_j \mathbf{x}_j^p \quad (7)$$

The particle filter ensures consistency among all the reconstructed variables as given by the climate model since only the weights of the particles are modified (and not directly the particles). In addition to the mean of the reanalysis, the Bayesian framework provides an estimation of the uncertainty of the reanalysis as well. Here, we define this uncertainty as the weighted standard deviation of the particles:

$$\sqrt{\sum_{j=1}^N w_j (\mathbf{x}_j^p - \overline{\mathbf{x}}^p)^2} \quad (8)$$

The DA process is executed over the complete period for which observations are available. Since we employ an offline DA method, each timestep of the DA is reconstructed independently. The assimilation is performed on anomalies, where the mean of both observations and model simulations is removed.

Large ensembles of Earth System Model simulations. The climate model used in the DA framework plays a pivotal role in the final reanalysis, as the modeled spatial covariance is employed to spread local observational information across space. Additionally, the modeled covariance between assimilated and reconstructed variables is used to reconstruct non-assimilated variables. To assess the influence of the choice of climate model within the DA framework on the final station-based reanalysis, we utilize 10 different Large Ensembles (LEs) generated by various Earth System Models (ESMs) (Table 1). For the paleo-based reanalysis, we exclusively use the last millennium ensemble (three simulations) performed with the isotope-enabled CESM1. This approach directly assimilates ice-core isotopic records, enhancing the skill of the reconstruction compared to the linear temperature- $\delta^{18}\text{O}$ relationship⁵⁰, thereby avoiding dependence on this non-stationary relationship⁵⁴. CESM1 has demonstrated good performance in reproducing atmospheric variability over Antarctica⁵⁵ as well as surface processes on the ice sheet⁵⁶, making it a reliable choice for this purpose.

Observation data. For the two atmospheric reanalyses, we use distinct observational datasets: instrumental observations for the station-based reanalysis and paleoclimate records for the paleo-based reanalysis. In both reconstructions, only observations from the mid- and high-latitude regions (45°S and beyond) are utilized. The locations of all records used in each reanalysis are displayed in Fig. 1.

Observations from weather stations. For instrumental observations, we exclusively use long-term near-surface air temperature and sea-level pressure records from weather stations located in the mid- and high-latitude regions of the Southern Hemisphere. Observations from Antarctic and sub-Antarctic weather stations were obtained from the READER dataset⁴², while mid-latitude observations originate from the University Corporation for Atmospheric Research (dataset ds570.0; see Fogt *et al.*⁵⁷ for further details). To prevent artefacts

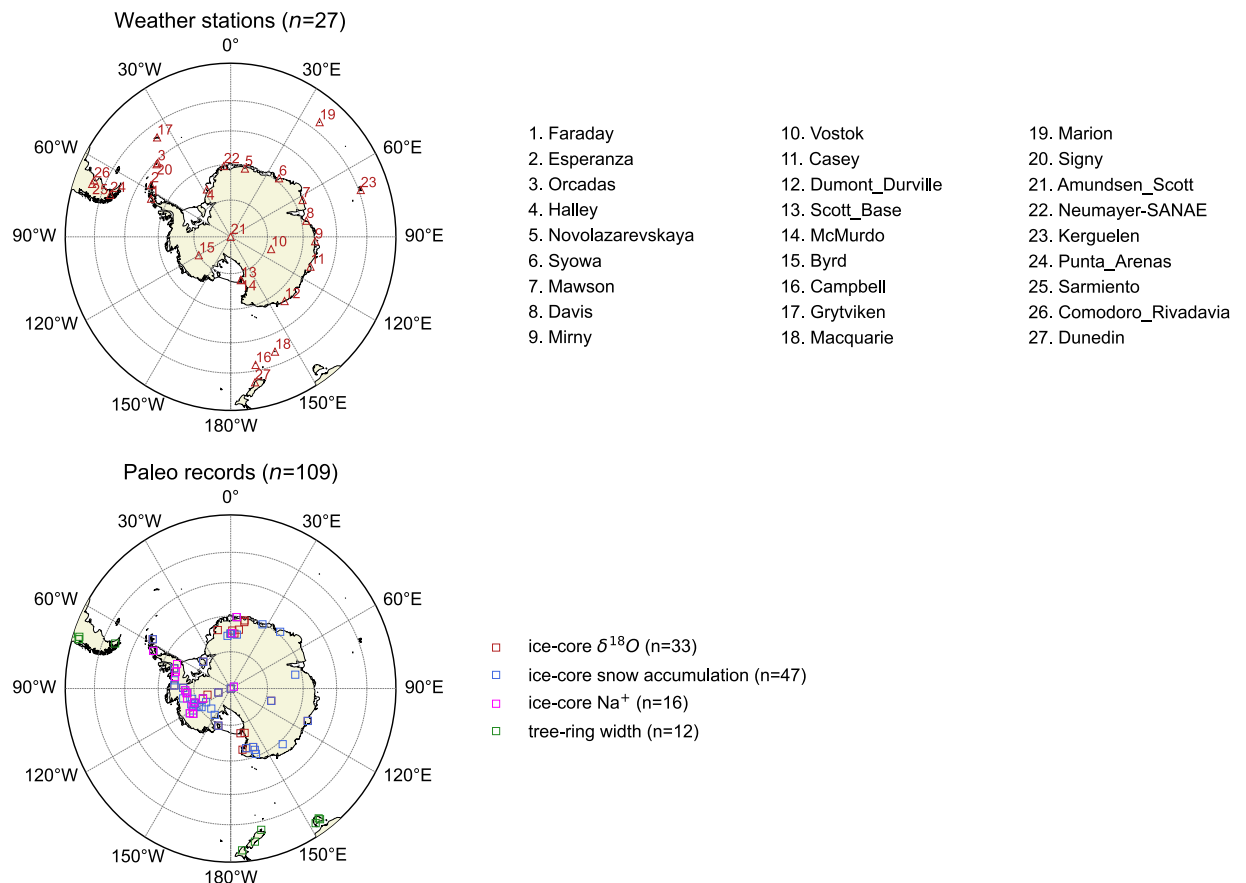


Fig. 1 Locations of the observations from weather stations and paleoclimate records used in the station- and paleo-based atmospheric reanalysis.

in the final reanalysis due to the increasing number of records over time, we chose to include only long-term records starting from 1961. In total, our dataset used for producing the station-based reanalysis includes 27 weather stations (Fig. 1). The records from the Antarctic and sub-Antarctic weather station data are accessible from the READER database (<https://legacy.bas.ac.uk/met/READER/>) and from the University Corporation for Atmospheric Research (dataset ds570.0; <https://rda.ucar.edu/datasets/ds570.0/#!description>).

Records from paleoclimate archives. Although we do not produce a new paleo-based atmospheric reanalysis, we provide details on the paleoclimate proxy records used in the paleo-based atmospheric reanalysis applied in this study^{31,58}. This reanalysis primarily relies on ice cores, supplemented by tree-ring width records. The inclusion of tree-ring records from mid-latitude regions helps to better constrain large-scale circulation patterns²⁹. For ice-core records, Dalaiden, Rezsóhazy *et al.*³¹ incorporated isotopic content^{59,60}, snow accumulation^{61,62}, the B40 snow accumulation records from Medley and Thomas¹³, and sea salt content^{63,64}. Only annually resolved records are used, resulting in a total of 109 records (Fig. 1). Compared to weather station observations, paleoclimate records are predominantly concentrated in the Pacific sector.

Forward operator. During the DA procedure, the model states (i.e., the prior) are compared with the available observations at each reconstructed time step. This process involves the forward operator (H in equation (2)), which projects the model states into the observational space. To prevent over-weighting regions with a high density of records, all records are first aggregated onto a polar stereographic grid of 500 km \times 500 km centered on Antarctica. These aggregated time-series are then used as observations in the DA process. For weather station observations, the comparison is direct, with model states interpolated onto the same 500 km \times 500 km grid. In the case of proxy records, however, the forward operator accounts for processes that govern the response of a sensor (for instance the width of a tree ring) to environmental conditions. In other words, the forward operator should capture all the relevant processes responsible for the observed variability in the proxy signal in the sensor. In paleoclimatology, this forward operator is commonly referred to as a Proxy System Model (PSM)⁶⁵. For isotopic content and snow accumulation in ice-core records, Dalaiden *et al.*²⁹ developed a PSM to account for representativeness errors – these errors arise from the coarse resolution of climate models and missing processes, which partly explain the model-observation discrepancy^{66,67}. Sea salt ice-core records, on the other hand, are assimilated as proxies for atmospheric circulation, more specifically to offshore changes in 500-hPa geopotential height based on the assumption that sea salt content reflects transport from the open ocean³¹. Finally, for

tree-ring width records, as in previous studies^{40,41,68}, a local linear PSM is applied, using local near-surface air temperature and/or precipitation (see Dalaiden *et al.*²⁹ for the exact implementation).

Oceanic reconstruction. *The ocean–sea-ice model: the NEMO – SI³ model.* Offline DA methods assume no temporal memory during the reconstructed period, as each time step is reconstructed independently. This approach is appropriate for atmospheric variables, where the time step of DA (i.e., one year) exceeds the predictability time for such variables (i.e., weak annual autocorrelation). However, this assumption is highly questionable for oceanic variables, particularly for the ocean at mid-depth, given the large inertia of the ocean. As a result, we cannot directly use the updated oceanic fields from the offline DA-based reanalysis. Instead, we employ an ocean model to reconstruct the ocean state, using our atmospheric reanalysis as the forcing for the model. The ocean model thus integrates atmospheric fluctuations to simulate the ocean state, ensuring temporal consistency.

Model configuration. We use NEMO 4.2⁶⁹ with a nominal resolution of 1° at the Equator (grid eORCA1) and 75 vertical levels, following a configuration similar to that of Hutchinson *et al.*⁴⁷. Given our focus on long-term changes at multi-decadal to centennial timescales, we opted for a global configuration, as these changes may be driven by large-scale fluctuations in ocean circulation, modifying water mass properties. Compared to previous eORCA1 configurations, Hutchinson *et al.*⁴⁷ included the explicit resolution of ocean circulation within ice shelf cavities developed in a quarter-degree NEMO configuration⁷⁰. Given the relatively low resolution of eORCA1 along the Antarctic coast, ocean circulation is explicitly resolved only within the three largest ice shelf cavities: the Ross Ice Shelf, Filchner-Ronne Ice Shelf, and Larsen C Ice Shelf. The resolution of the ocean circulation in these cavities was, partly, necessary to prevent unrealistic intrusions of warm water masses towards the Ross Ice Shelf. The bathymetry is a combined dataset derived from Earth Topography version 2⁷¹ and the International Bathymetric Chart of the Southern Ocean⁷² for sub-ice shelf bathymetry. Further details on the implementation of ice shelf cavity openings can be found in Hutchinson *et al.*⁴⁷. NEMO is coupled with the SI³ sea-ice model, which resolves both the thermodynamics and dynamics of sea ice^{73,74}. Additional details on the numerical schemes and parameter values can be found in the simulation namelists provided in the Supplementary Materials.

The initial conditions for each NEMO – SI³ simulation are based on the 1981–2010 climatology from the World Ocean Atlas 2013 (WOA2013)^{75,76}, unless otherwise specified. Since WOA2013 does not provide the necessary fields within ice shelf cavities, Hutchinson *et al.*⁴⁷ conducted regional simulations for the three major ice shelves using NEMO, with boundary conditions derived from WOA2013. We therefore utilize these spatially extended fields as initial conditions for our simulations (see Hutchinson *et al.*⁴⁷ for further details). In the three resolved ice shelf cavities, the freshwater flux from ice shelf melting is directly computed within NEMO (see Hutchinson *et al.*⁴⁷ for details of the calculation). The freshwater flux in other cavities is imposed from Depoorter *et al.*⁷⁷ and remains constant over time. A sea surface salinity restoring is applied in all simulations, nudging towards the 1981–2010 WOA2013 climatology, except under sea ice. Although this restoring was necessary to prevent a salinity drift and the formation of large open-sea polynyas in the Weddell Sea, this might partly suppress variability in the model, particularly on long timescales.

Long-term atmospheric forcing and methodology for building the atmospheric forcing. Since we use a NEMO – SI³ configuration without atmospheric coupling (standalone configuration), it is necessary to prescribe air–sea fluxes. Specifically, NEMO – SI³ requires several atmospheric forcing variables at the surface, including sea-level pressure, near-surface air temperature, total and solid precipitation, meridional and zonal wind components, shortwave and long-wave radiation fluxes, and near-surface specific humidity. NEMO – SI³ requires high temporal frequency atmospheric forcing. However, both the station-based reanalysis and paleo-based reanalysis are only available at annual resolution. Additionally, these two reanalyses cover only the Southern Ocean. In this section, we describe the method used to generate a transient global atmospheric forcing dataset at 6-hourly resolution for the period 1700–2023.

Global atmospheric reanalysis over the past centuries. Since both the station and paleo-based reanalysis only cover the high latitudes of the Southern Hemisphere and we employ a global ocean configuration, an atmospheric forcing outside of the Southern Ocean is needed. We use the Modern Era Reanalysis (Mode-RA)⁴¹ for the global pre-satellite atmospheric reanalysis. Mode-RA combines instrumental measurements, documentary data, paleoclimate records, and climate model simulations through a DA method. As Mode-RA provides time anomalies, we recompute the climatology over 1981–2010 and add the corresponding climatology from the latest ECMWF atmospheric reanalysis (ERA5)⁷⁸, so that the mean state is bias-corrected based on ERA5. The temporal resolution of Mode-RA is monthly; however, we compute the annual mean to keep consistency with the station and paleo-based reanalysis. In contrast to our reanalyses, Mode-RA does not provide all the necessary atmospheric fields to force the NEMO – SI³ model. Specifically, surface winds, specific 2-m humidity, and long-wave and short-wave radiation fluxes are not provided. Consequently, we derive these variables from the available fields in Mode-RA. For surface winds, Mode-RA provides zonal and meridional winds at 850 hPa. To obtain winds at the surface, we apply spatially dependent scaling factors to the two wind components at 850 hPa. These scaling factors are computed by comparing the wind components at the surface and 850 hPa in ERA5. For 2-m specific humidity, we assume that monthly relative humidity remains constant over time, based on the present-day conditions. We first compute the monthly climatology of near-surface air temperature, specific 2-m humidity, and sea-level pressure from ERA5. From these, we derive the monthly climatology of relative humidity following the Clausius–Clapeyron relation (approximated based on the formula of Tetens). Then, using reconstructed monthly near-surface air temperature and sea-level pressure, we compute the monthly 2-m saturation specific humidity and apply the fixed relative humidity to obtain 2-m specific humidity over the full

reconstruction period. This approach ensures that specific humidity evolves consistently with temperature and pressure changes, while maintaining a constant relative humidity. This assumption is reasonable for non-limiting moisture regions, such as oceans. The consideration of long-wave radiation flux changes is crucial. The change in long-wave radiation flux (ΔLW) can be expressed as a temperature change (ΔT), specifically as the first term in the Taylor expansion of the Stefan-Boltzmann Law:

$$\Delta LW \approx 4 \sigma \epsilon \overline{T^3} \Delta T \quad (9)$$

where σ is the Stefan-Boltzmann constant (5.670373×10^{-8} ; $\text{W} \cdot \text{m}^{-2} \cdot \text{K}^{-4}$) and ϵ is the atmospheric emissivity. Using the Stefan-Boltzmann Law, we estimate a spatially dependent atmospheric emissivity based on ERA5. Although the atmospheric emissivity varies annually (e.g., due to changes in cloud cover), we assume a constant value over time. We do not account for changes in short-wave radiation flux for regions outside of the Southern Ocean, as Mode-RA does not provide relevant variables (the 1981–2010 climatology from ERA5 is used).

The final atmospheric forcing used to drive NEMO – SI³ is a merged product derived from the station-based reanalysis, paleo-based reanalysis, Mode-RA, and ERA5. For the period 1700–1957, the paleo-based reanalysis is merged with Mode-RA between 42°S and 52°S using a cosine-weighted scheme. For the period from 1958 onward, the station-based reanalysis is merged with ERA5 with the same merging between 42°S and 52°S. For consistency with the paleo-based reanalysis, we selected the station-based reanalysis relying on CESM1 for building the prior. This results in a global atmospheric forcing dataset spanning from 1700 to the present. To assess the performance of the paleo-based reanalysis, we evaluate the skill of key atmospheric variables (temperature, precipitation, and winds) against both ERA5 and the station-based reanalysis.

Downscaling annually-resolved reanalysis for high-temporal atmospheric forcing. NEMO – SI³ requires atmospheric forcing inputs every 6 hours to account for, for instance, the influence of the diurnal cycle. However, our reanalyses are only available at annual resolution. Therefore, to obtain a high-temporal atmospheric forcing, we process as follows: 1. we downscale the annually-resolved reanalysis to the monthly resolution (monthly downscaling); 2. we apply a seasonal bias correction based on ERA5 (seasonal bias correction); 3. we add the high-frequency variability (i.e., weather variability) from ERA5 (high-frequency variability).

Monthly downscaling. As our reanalyses provide annual anomalies, we must distribute these anomalies across individual months. In other words, we need to determine how the annual anomaly is expressed throughout the year. For example, at high latitudes, shortwave radiation flux anomalies should occur during summer months. To achieve this, we quantify the typical monthly distribution of anomalies in each variable using ERA5. Specifically, we compute monthly spatial-dependent scaling factors (β_m , with $m = 1, \dots, 12$) that are proportional to the deviation of the monthly value from its monthly climatology, relative to the deviation of the annual value from its annual climatology. The scaling factors are computed based on ERA5 data over the 1979–2022 period, and are defined as:

$$\beta_m = \alpha \cdot \frac{\sigma_{var,m}}{\sigma_{var,y}} \quad \text{with} \quad \alpha = \frac{12}{\sum_{m=1}^{12} \frac{\sigma_{var,m}}{\sigma_{var,y}}} \quad (10)$$

where $\sigma_{var,m}$ and $\sigma_{var,y}$ are the standard deviations of the monthly and annual values, respectively, for each forcing variable (*var*). These monthly scaling factors are then used to downscale the annual anomalies from the reanalysis to monthly anomalies as follows:

$$ANO_m = \beta_m \cdot ANO_y \quad (11)$$

where ANO_y is the annually-resolved anomaly from the reanalysis, and ANO_m is the resulting monthly anomaly. As a result, months that contribute more significantly to the annual variability receive proportionally larger anomalies. This approach allows us to generate a monthly reconstruction (LF_{rec}) for both the station and paleo-based reanalysis.

Seasonal bias correction. To convert anomaly fields into absolute fields, we add a reference monthly climatology to the monthly reconstruction (i.e., LF_{rec}). The monthly climatology is computed from ERA5 over the 1981–2010 period and smoothed using a cubic spline, denoted as LF_{clim} . This ensures that the reconstructed forcing has zero bias relative to ERA5, by construction.

High-frequency variability. To incorporate high-frequency variability over the monthly signal provided by LF_{rec} , we derive this variability from ERA5, assuming that changes in the climate background have minimal impact on sub-monthly variability. For this purpose, we follow the methodology outlined in a modeling study that projected future oceanic conditions based on CMIP models⁷⁹. To generate high-frequency variability, we follow the approach presented in Naughten *et al.*⁷⁹, which utilizes multiple decades to construct high-frequency atmospheric variability. This method is particularly relevant for regions like Antarctica, where natural variability is strong²⁶. We use the 1981–2010 period to build the high-frequency variability at 6-hourly resolution. First, we subtract the monthly mean from the 6-hourly time series of ERA5 forcing data. To ensure a smooth transition between months, we apply a cubic spline to the monthly-mean time series. As a result, the derived 6-hourly time series from 1981–2010 (30-year long) represents high-frequency variations without the monthly signal (HF_{ctrl}).

The final atmospheric forcing is then obtained as the sum of LF_{rec} , HF_{ctrl} , and LF_{clim} . HF_{ctrl} is cyclically repeated over the period covered by the atmospheric forcing (i.e., 1700–2023).

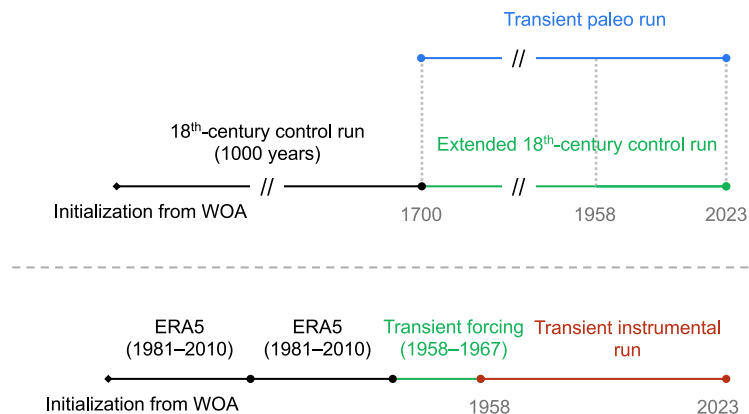


Fig. 2 Setup of the NEMO – SI³ simulations presented in the study.

When constructing the atmospheric forcing, some variables may exhibit non-physical values, particularly precipitation, specific humidity and short- and long-wave fluxes, where negative values can occasionally be observed. To ensure the conservation of the annual anomaly, we set the time steps displaying negative values to zero and apply a scaling factor to the other time steps. This scaling factor is defined as the ratio of the sum of negative values to the sum of positive values (i.e., we reduce the positive values by this scaling factor). For near-surface specific humidity, a similar correction is applied by ensuring that the relative humidity does not exceed 100%. When this occurs, the near-surface specific humidity is adjusted to correspond to 100%. For all other time steps, the near-surface specific humidity is increased to maintain the same annual anomaly.

Experimental design of oceanic simulations. The experimental design of the NEMO – SI³ simulations is outlined in Fig. 2. To force NEMO – SI³ with a transient atmospheric dataset covering the past 300 years, we must start from pre-industrial conditions. Therefore, we first performed a 1000-year control simulation under 18th-century climate conditions. Specifically, the period 1701–1730 (considered as representative of the 18th century atmospheric conditions) from the atmospheric forcing dataset was cyclically repeated over 1000 years, ensuring sufficient time for the model to reach equilibrium and prevent drift in the subsequent transient simulation. This control simulation was initialized from WOA2013^{75,76} (see the section dedicated to the model configuration). The final state of the control run was then used to initialize NEMO – SI³ for a transient simulation spanning the period 1700–2023. This simulation is driven by the entire atmospheric forcing that includes both the paleo and station-based reanalysis as discussed in the section focused on the creation of the atmospheric forcing. This simulation is referred to as the transient paleo simulation. We also conduct an additional NEMO – SI³ simulation over 1958–2000 using only the paleo-based reanalysis as atmospheric forcing. Additionally, the control simulation was extended for the same duration as the transient simulation to verify the absence of model drift. To complement the transient paleo simulation, we also performed an additional NEMO – SI³ simulation over the period 1958–2023, initialized from the *present-day* conditions. For this setup, we followed the methodology of Goosse *et al.*⁴³: NEMO – SI³ was first initialized from WOA2013 and forced with ERA5, repeating the 1981–2010 period twice. This was followed by a 10-year spin-up phase using the 1958–1967 transient atmospheric forcing, allowing for a smoother transition when initializing the model in 1958. Finally, the model was run from 1958 until 2023 using the transient atmospheric forcing. This simulation is referred to as the transient instrumental simulation. Comparing the two NEMO – SI³ simulations enables us to assess the influence of past climate variability on variability observed during 1958–2023.

Data Records

The dataset is available at Zenodo <https://zenodo.org/records/15472051>⁸⁰. The archive includes atmospheric reanalyses at annual resolution, covering key surface climate variables: sea-level pressure, surface meridional and zonal winds, 2-m air temperature, precipitation, and sea-ice concentration, as well as regional Antarctic sea-ice extent. These are provided for both the station-based and paleo-based reanalyses, with associated uncertainty estimates, and are expressed as anomalies relative to 1981–2010 period and 1961–1990 period for the station-based and paleo-based reanalysis, respectively. For the station-based reanalysis, we provide both the ensemble mean (averaged across all reanalyses using different climate model priors) and each individual reanalysis. The monthly atmospheric forcing used to drive the ocean model is also included (expressed in absolute values). For the oceanic simulations from the transient paleo and instrumental experiments, the archive provides annual outputs of key physical variables - temperature, salinity, zonal and meridional currents, sea-ice concentration, and barotropic streamfunction - restricted to the Southern Ocean. Monthly sea-ice concentration fields are also included. All the variables from the oceanic simulations are expressed in absolute values. Each file (in NetCDF) follows a consistent naming convention and includes metadata to clarify its contents.

Technical Validation

To assess the skill of the atmospheric and oceanic reconstruction, we compare them with various existing observations and reconstructions. We mainly use three skill metrics. Ability to capture variability is quantified using the linear Pearson correlation coefficient (r). Absolute skill is quantified using the Relative Root Mean Square Error (RRMSE; %) defined as:

$$RRMSE = \sqrt{\frac{\sum_{i=1}^n (y'_i - x'_i)^2}{\sum_{i=1}^n (y'_i)^2}} \times 100 \quad (12)$$

where $'$ indicates departures from the time mean, n is the number of samples (e.g., the length of the time series), y represents the predicted values (e.g., the reanalysis), and x corresponds to the observational dataset. Low RRMSE values indicate low errors. We also quantify the ensemble spread to ensure the ensemble encompasses the reconstruction error (i.e., the difference between the reconstruction and the observation dataset) by computing the Ensemble Calibration Ratio (ECR), defined as:

$$ECR = \frac{1}{n} \sum_{i=1}^n \frac{(y'_i - x'_i)^2}{\sigma_{y,i}^2} \quad (13)$$

where $\sigma_{y,i}^2$ is the variance of the ensemble of the reconstruction at time i . An ECR value of unity indicates that the ensemble is correctly calibrated, meaning that it has sufficient spread to account for the reconstruction error. Higher (lower) values indicate an underdispersive (overdispersive) ensemble, implying that the ensemble underestimates (overestimates) the error (i.e., the difference between the reconstruction and the observation dataset). In general, ECR values higher than unity are less desirable than values lower than unity, as they indicate that the estimated reconstruction uncertainty is too small to encompass the actual error.

Atmospheric reanalysis. *Station-based reanalysis.* Figure 3 presents the maps of annual correlation coefficients between the station-based reanalysis and ERA5 for near-surface air temperature, sea-level pressure, precipitation, and zonal and meridional surface winds over 1979–2023. As highlighted in Goosse *et al.*⁴³, the station-based reanalysis exhibits strong agreement with ERA5 for near-surface air temperature ($\bar{r} = 0.64$; for latitudes poleward of 50°South) and sea-level pressure ($\bar{r} = 0.82$) across the mid- to high-latitude regions of the Southern Hemisphere. Despite no direct precipitation observations being used in the station-based reanalysis, the reanalysis demonstrates decent skill in reproducing precipitation patterns ($\bar{r} = 0.47$), particularly over the Southern Ocean near the Antarctic coast, as well as over the West Antarctic Ice Sheet and the Antarctic Peninsula. Regarding surface winds, the station-based reanalysis performs well, with correlation coefficients of $\bar{r} = 0.61$ and $\bar{r} = 0.67$ for zonal and meridional surface winds, respectively. The agreement is particularly strong over the ocean, though performance declines in specific coastal regions, such as Dronning Maud Land, where both zonal and meridional wind correlations are lower. This discrepancy may be attributed to the complex orography of the East Antarctic Ice Sheet as well as the presence of strong katabatic winds⁸¹. It is important to acknowledge that the evaluation of the reanalysis is performed using ERA5 as the observational reference. However, ERA5 is itself subject to biases. Nevertheless, among state-of-the-art atmospheric reanalysis products, ERA5 has been shown to exhibit comparatively lower biases relative to in situ and satellite-based observations over the Antarctic Ice Sheet^{81,82}.

Table 2 presents the three skill metrics for the Southern Annular Mode (SAM), integrated near-surface air temperature and precipitation over the four main sub-Antarctic regions (West Antarctic Ice Sheet, East Antarctic Ice Sheet, Antarctic Peninsula and Antarctic Ice Sheet as a whole), as well as regional sea-ice extents. The time evolution of the SAM, a key metric related to the westerly wind variability⁸, is evaluated against the station-based Marshall index⁸³ over 1958–2023 and is well reproduced ($r = 0.90$; RRMSE = 5.46%; ECR = 0.74). The mean value of ECR, being lower than unity indicates that the ensemble is correctly calibrated and accounts for reconstruction error (i.e., the difference between the station-based reanalysis and observations). Additionally, the ensemble spread among all the reanalysis based on different model prior for r and RRMSE is small, suggesting that the choice of the ESM in DA has little impact, the observational network contributing the most. For integrated near-surface air temperature over the four sub-Antarctic regions, the station-based reanalysis demonstrates strong performance (as already observed in Fig. 3), with a correlation coefficient of 0.92 for Antarctica as a whole, an RRMSE of 6.07%, and an ensemble that remains correctly calibrated since the mean ECR is lower than unity. In contrast, precipitation shows weaker skill ($r = 0.55$; RRMSE = 12.62% for Antarctica as a whole), though better performances for the Antarctic Peninsula. The mean ECR is larger than unity, suggesting that the ensemble underestimates the error. Overall, the ensemble spread is also larger compared to SAM and regional temperature, which is expected since precipitation observations are not assimilated, making the simulated covariance of the ESM having a central role in the final reanalysis. Additionally, although ERA5 demonstrates good performance over Antarctica for near-surface air temperature and winds^{81,82}, precipitation estimates are associated with larger uncertainties. These biases may partly account for the lower agreement observed between ERA5 and the station-based reanalysis for precipitation compared to other variables. Therefore, we repeated the evaluation using the polar-oriented Regional Atmospheric Climate Model RACMO2.3p2⁸⁴, which has been extensively evaluated and is considered a reliable benchmark for surface mass balance components over the Antarctic Ice Sheet. Results show similar results using ERA5 ($\bar{r} = 0.55$, RRMSE = 12.81% and ECR = 1.92 for Antarctica as a whole). Finally, regional sea-ice extents are relatively well captured across all regions, despite the

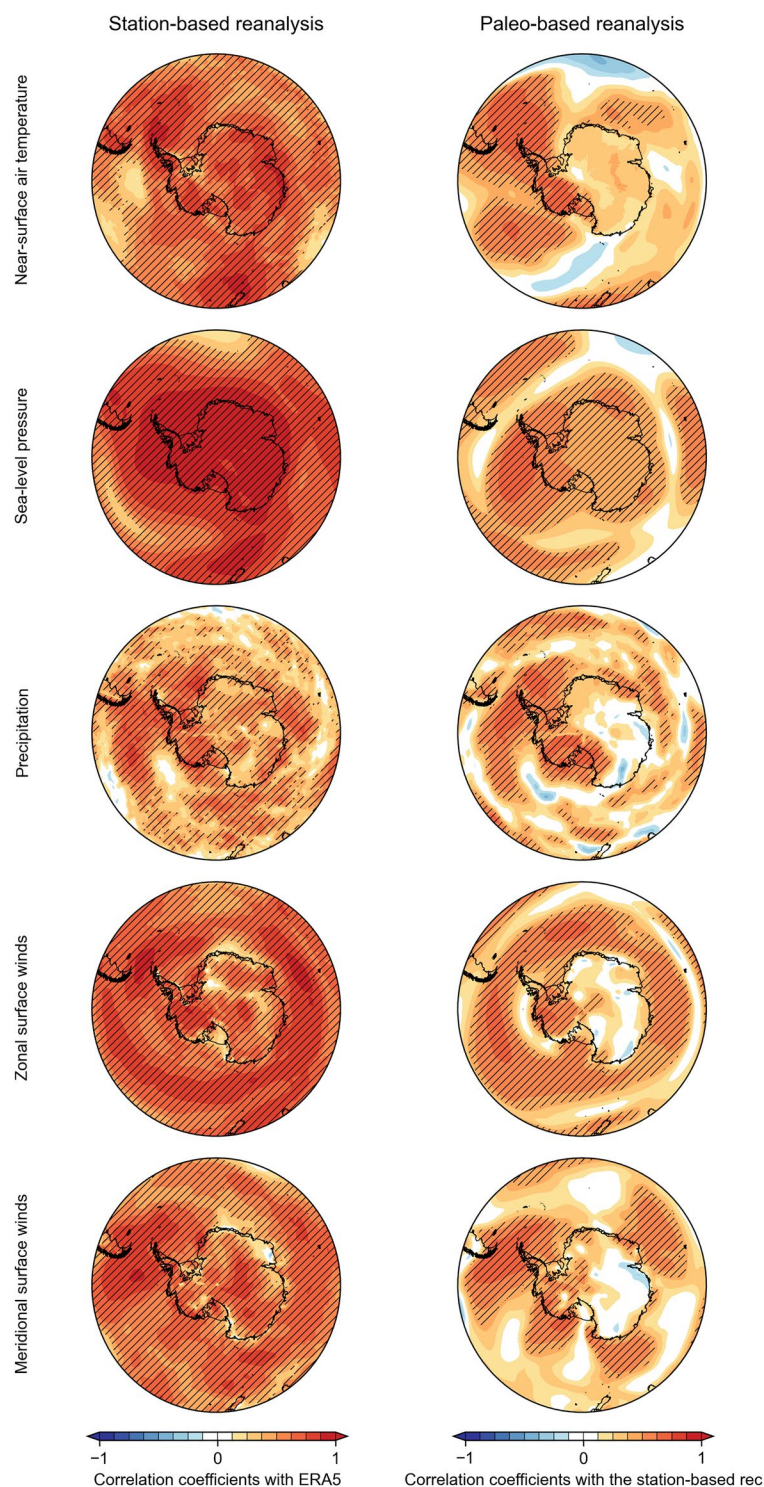


Fig. 3 (left) Annual correlation coefficients between the station-based reanalysis and ERA5 over 1979–2023 for near-surface air temperature, sea-level pressure, total precipitation, and zonal and meridional surface winds. (right) Correlation coefficients between the station-based reanalysis and the paleo-based reanalysis over 1958–2000 for the same variables.

absence of direct sea-ice observations in the assimilation process. Notably, the Weddell and Bellingshausen/Amundsen seas show good skill ($r = 0.71$ and $r = 0.67$, respectively), with RRMSE values remaining consistent across all regions (approximately 12%). ECR values indicate that the ensemble effectively accounts for model uncertainty. Further validation for sea ice is provided in the section assessing the historical variability of the ocean.

	<i>r</i>	RRMSE [%]	ECR
Atmospheric modes			
Southern Annular Mode	0.90* \pm 0.01	5.46 \pm 0.24	0.74 \pm 0.25
Near-surface air temperature			
West Antarctic Ice Sheet	0.78 * \pm 0.05	9.56 \pm 0.71	0.58 \pm 0.13
East Antarctic Ice Sheet	0.92 * \pm 0.02	6.39 \pm 0.54	0.88 \pm 0.33
Antarctic Peninsula	0.88 * \pm 0.03	7.39 \pm 0.71	0.46 \pm 0.27
Antarctic Ice Sheet	0.92 * \pm 0.02	6.07 \pm 0.67	0.66 \pm 0.30
Precipitation			
West Antarctic Ice Sheet	0.68 * \pm 0.05	11.45 \pm 0.54	1.18 \pm 0.47
East Antarctic Ice Sheet	0.65 * \pm 0.07	12.18 \pm 0.58	1.87 \pm 0.79
Antarctic Peninsula	0.86 * \pm 0.03	10.43 \pm 0.51	3.70 \pm 2.41
Antarctic Ice Sheet	0.55 * \pm 0.10	12.62 \pm 0.85	1.90 \pm 0.91
Sea ice			
Bellingshausen/Amundsen Sea	0.71 * \pm 0.12	10.75 \pm 1.57	0.37 \pm 0.27
Weddell Sea	0.67 * \pm 0.05	11.08 \pm 0.64	0.95 \pm 0.38
King Hakon	0.59 * \pm 0.14	12.10 \pm 1.75	0.75 \pm 0.90
East Antarctica	0.55 * \pm 0.06	12.83 \pm 0.80	0.82 \pm 0.63
Ross Sea	0.57 * \pm 0.16	12.45 \pm 1.66	0.67 \pm 0.43
Southern Ocean	0.55 * \pm 0.09	12.67 \pm 0.77	0.79 \pm 0.47

Table 2. Evaluation metrics for the annually resolved station-based atmospheric reanalysis for the Southern Annular Mode (compared against the Marshall index⁸³ over 1958–2023), regional near-surface air temperature and precipitation (compared against ERA5 over 1979–2023), and regional sea-ice extent (compared with NSIDC³ over 1979–2023). The definitions of the regions for near-surface air temperature and precipitation follow Steig *et al.*¹²²: the West Antarctic Ice Sheet (60–180°W, south of 72°S), the East Antarctic Ice Sheet (60°W–180°E), and the Antarctic Peninsula (60–180°W, north of 72°S). The five sea-ice extent regions are defined as follows: Amundsen/Bellingshausen Seas (110°W–70°W), Weddell Sea (70°W–15°W), King Hakon sector (15°W–70°E), Indian sector (70°E–165°E), and Ross Sea (165°E–110°W). Correlation coefficients (*r*), RRMSE, and ECR values are presented for the multi-model ensemble mean, along with the standard deviation of the multi-model ensemble. Statistically significant correlations at the 95% confidence level are marked with stars.

Finally, we evaluate the reconstructed temperature at the weather station locations where observations are assimilated by comparing them with these observations and ERA5 (Fig. 4). For the 22 assimilated temperature time series, the station-based reanalysis successfully reproduces the observed temperature variability ($\bar{r} = 0.82$), except at Marion Island, where it fails to capture the warming trend from 1958 to the early 21st century. The anomalously low reconstructed temperature at the Marion Island location is likely due to the limited spatial extent of the sub-Antarctic island, which prevents the model from adequately capturing the thermal contrast between land and surrounding ocean. In contrast to the station-based reanalysis, ERA5 simulates a pronounced warming over 1958 to the beginning of the satellite period (i.e., 1979) for several East Antarctic locations, including Novolazarevskaya, Mawson, Davis, Dumont d’Urville, Neumayer-SANAE, and McMurdo (see Fig. 1 for specific locations). This aligns with recent findings⁸⁵, which highlight substantial temperature biases in ERA5 before the satellite era. Similar biases are also evident in ERA5 for atmospheric pressure (Fig. S1).

Paleo-based reanalysis. Since the skill of the paleo-based reanalysis has already been extensively evaluated in Dalaiden *et al.*²⁹ and Dalaiden, Rezsóhazy *et al.*³¹, we only provide a brief summary here. The performance of the paleo-based reanalysis is assessed by comparing it with the station-based reanalysis over the 1958–2000 period, as the overlap with ERA5 (1979–2000) is too short for a robust evaluation. Overall, the paleo-based reanalysis shows good agreement with the station-based reanalysis for sea-level pressure, near-surface air temperature, precipitation and winds in the Atlantic and Pacific sectors, while a much larger disagreement is noticed in the East Antarctic sector (Fig. 3). This reduced skill in East Antarctica, also reported in other paleo-based reconstructions using similar methods^{30,86}, is primarily associated with the limited number of records in this region, the higher noise in ice-core records (often located in low-accumulation zones), and the complex topography, which coarse-resolution climate models struggle to represent accurately. Reconstructed sea-ice extent is discussed later in the section related to the historical variability of the ocean. For a more detailed evaluation, we also refer the reader to Dalaiden *et al.*²⁹ and Dalaiden, Rezsóhazy *et al.*³¹, as well as Goosse *et al.*⁴³ for the reconstructed sea-ice extent from the paleo- and station-based atmospheric reanalyses.

Oceanic reanalysis. *Overall representation over present-day conditions.* Before evaluating the historical variability of the Southern Ocean over the past centuries, we first assess whether NEMO – SI³, when forced by the reconstructed atmospheric forcing, accurately reproduces the mean state of main oceanic features. Figure 5 presents the 1981–2010 climatology of the barotropic stream function from both the transient instrumental and

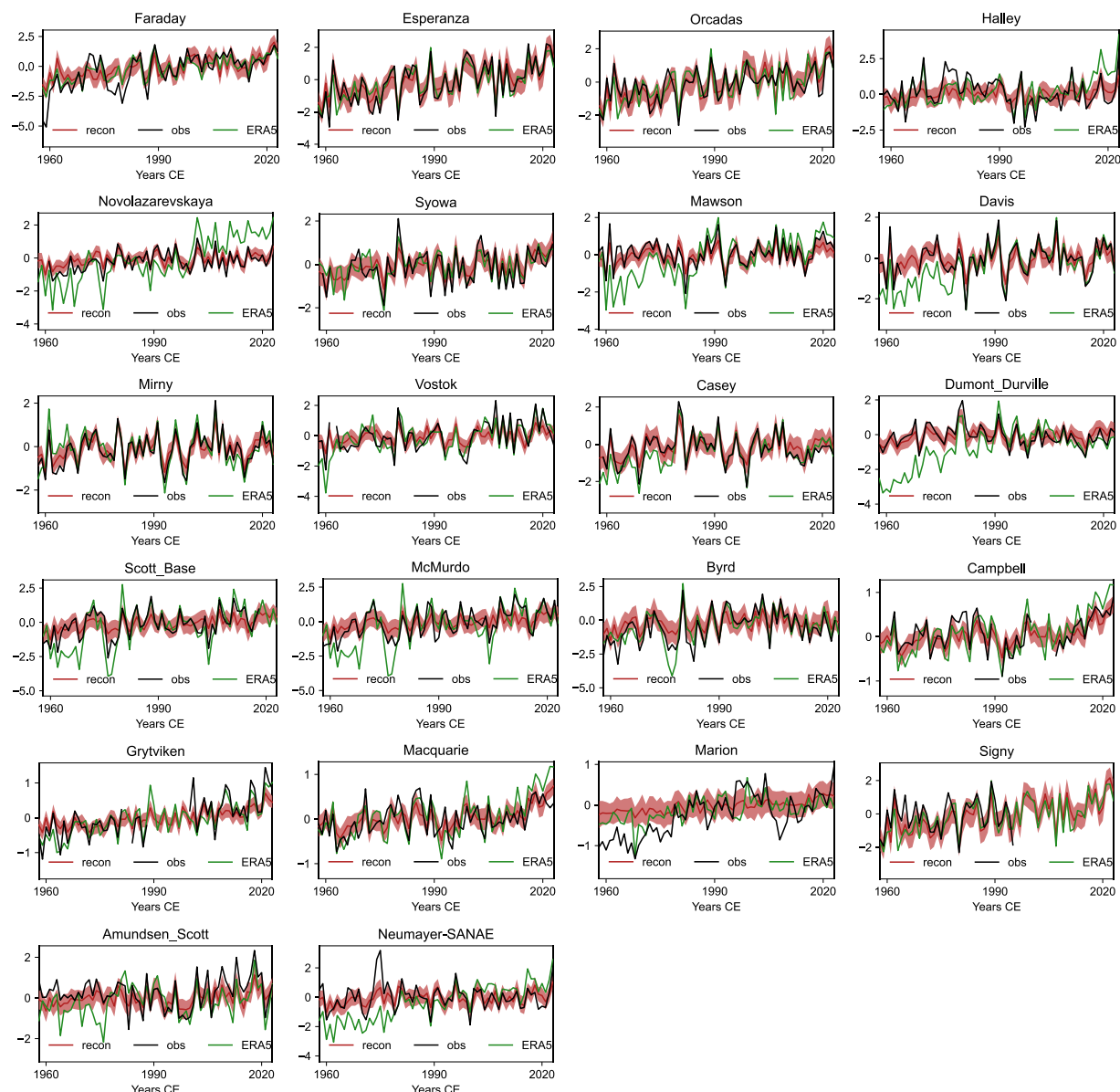


Fig. 4 Annual time series of near-surface air temperature (relative to the 1958–2023 period; in °C) from Antarctic and sub-Antarctic weather stations over 1958–2023, based on observations (*obs*; black), the station-based reanalysis (*recon*; red), and ERA5 (green). The red shading represents one standard deviation of the ensemble of the station-based reanalysis. The geographical locations of each weather station are shown in Fig. 1.

paleo simulations, along with temperature and salinity at seabed, compared against WOA2013^{75,76}, which is used as the observational reference dataset.

Albeit in both simulations, the barotropic stream function follows the general path of the Antarctic Circumpolar Current (ACC)⁸⁷ and both simulations capture the Weddell and Ross gyres (negative values of the barotropic stream function indicate a clockwise circulation), the Ross Gyre extends farther into the Amundsen Sea and northward in the transient instrumental simulation, differing from previous studies⁸⁸. The ACC transport through Drake Passage is 118 Sv in the transient instrumental simulation and 144 Sv in the transient paleo simulation. The latter is in better agreement with the observed values (137–173 Sv^{89,90}, but in the low range) and the estimated transport of approximately 155 Sv from two oceanic reanalyses^{91,92}. We also notice weaker Ross and Weddell gyres in the transient paleo simulation (20 Sv and 40 Sv, respectively; defined as the maximum barotropic stream function in the two areas) compared with the transient instrumental simulation (34 Sv and 48 Sv, respectively). The transient paleo simulation is in better agreement with the Southern Ocean State Estimate⁹¹, with transport values of 20 ± 5 Sv and 40 ± 8 Sv for the Ross and Weddell gyres.

The simulated temperature at seabed shows overall good agreement with observations, capturing key thermal structures such as warm water masses over the continental shelf in the Amundsen and Bellingshausen Seas (though slightly overestimated) and colder conditions in East Antarctica (Fig. 5). Cold conditions are also observed in the Weddell and Ross Seas and their surroundings. As a note, the transient paleo simulation has

a cold bias over the continental slope in East Antarctica. This bias could be related to the fresh bias and to the coarse spatial resolution on these narrow ice shelves. However, uncertainties in the observational dataset are also important in that sector⁹³.

Salinity plays a critical role in accurately simulating global oceanic circulation. In the high-latitude Southern Ocean, the formation of High Salinity Shelf Water (HSSW) on the continental shelves - particularly in the Ross and Weddell Seas - is a key precursor to the production of Antarctic Bottom Water. Compared to the WOA, the salinity at seabed from the transient instrumental simulation shows a strong fresh bias over the continental shelves, especially in the western Ross and Weddell Seas, which limits HSSW formation. In contrast, the transient paleo simulation exhibits a much smaller bias (around 0.04 g kg^{-1}), likely due to its longer integration time (1,400 years), which allows the deep ocean to reach a more stable and physically consistent state. However, the transient paleo simulation still presents a fresh bias over the East Antarctic shelf, potentially due to the absence of coastal polynyas formed by landfast ice⁹³. Additionally, a fresh bias is noticed in the deep ocean (approximately 0.09 g kg^{-1}), which may be attributed to model drift.

Finally, regarding sea ice, both the transient instrumental and paleo simulations accurately reproduce the main observed annual sea-ice concentration pattern (Fig. 6) as well as the total annual Antarctic sea-ice extent ($13.2 \times 10^6 \text{ km}^2$ and $11.7 \times 10^6 \text{ km}^2$, respectively), which aligns well with satellite-based observations of $12.6 \times 10^6 \text{ km}^2$ ²³. During the austral winter, the simulations closely match observations, whereas in the austral summer, it tends to underestimate the observed sea-ice cover, especially in the Indian sector where the simulations display no ice. As noted for the salinity bias, the lack of sea ice in the Indian sector may be linked to the non-resolution of landfast ice in our simulations.

Historical Southern Ocean Sea Surface Conditions since 1700. As the presented NEMO – SI³ simulations are not coupled to the atmosphere, we expect that the sea surface conditions are similar to the atmospheric forcing, in particular for the sea-ice cover because the fingerprint of the sea-ice edge is present in the near-surface air temperature fields used in the atmospheric forcing. However, NEMO – SI³ may bring additional information to the simulated sea surface conditions, related to the contribution of oceanic processes, which might thus result in different sea surface conditions.

Sea Surface Temperature. For sea surface temperature (SST), we compare our simulations with OISST⁹⁴, which is based on in-situ oceanic observations and satellite observations. For the earlier period, we also use ERSSTv5⁹⁵. However, ERSSTv5 exhibits substantial biases prior to 1980 at high southern latitudes due to the scarcity of observations, relying almost entirely on spatial interpolation from lower latitudes. Unlike OISST, ERSSTv5 does not incorporate satellite observations. Figure 7 presents the time series of annual SST averaged over the Southern Ocean (50° – 60° S) from OISST, ERSSTv5 and the two NEMO – SI³ simulations. As expected, the two simulations are very similar to each other, explained by the common atmospheric forcing and the surface salinity restoring. Overall, the simulations are consistent with OISST, capturing the observed cooling from 1982 to around 2000, followed by a subsequent warming trend to the present (albeit underestimated). Additionally, the simulations show a warming period from 1958 to 1980, a cooling phase until approximately 2000, and a warming thereafter, reflecting pronounced multi-decadal variability. In contrast, ERSSTv5 exhibits a stronger amplitude of variability, with a more pronounced warming prior to 1980 and a sustained cooling until about 2010. This discrepancy may stem from larger uncertainties in ERSSTv5 during this period, as well as uncertainties in the sea-ice mask applied to SST products, which is particularly uncertain before 1979⁹⁵, and may influence SST estimates further north. Prior to 1958, SST products over the Southern Ocean are highly uncertain, making it difficult to draw robust conclusions about long-term variability.

Sea-ice extent. To assess historical sea-ice extent variability in the two NEMO – SI³ simulations, we first compare them with the reconstructed sea-ice extent derived from the atmospheric reanalysis, which serves as the atmospheric forcing for the simulations (Fig. 8). The differences between the two highlight the influence of ocean dynamics on sea-ice changes. We then evaluate our NEMO – SI³ simulations against the satellite-based NSIDC product^{3,96} for the 1979–2023 period. For the 20th century, we compare our results to the reconstruction of Fogt *et al.*⁵⁷. This reconstruction is based on mid-latitude atmospheric teleconnections linking atmospheric pressure and near-surface air temperature from long-term weather stations as well as climate mode indexes to regional and Antarctic-wide sea-ice extent at the seasonal timescale.

During the satellite period, all the reconstructions show relatively good agreement with the observations (Fig. S2), although they struggle to reproduce the total sea-ice extent maximum observed in 2014, mainly arising from an underestimation of the reconstructed sea-ice expansion in the King Håkon and Indian sectors as well as the Weddell Sea. Regarding the 1979–2014 period, the instrumental and paleo simulations virtually exhibit no trend in total Antarctic sea-ice extent compared to the positive, statistically significant trend from NSIDC. As highlighted in Goosse *et al.*⁴³, this discrepancy primarily results from an underestimation of the 2014 sea-ice maximum in both simulations. Additionally, the paleo simulation exhibits a pronounced sea-ice minimum around 2003 in the Bellingshausen/Amundsen and King Håkon sectors (in contrast with satellite-based observations and instrumental simulation), contributing to a delayed recovery and weaker trend over the period. This behavior underscores the influence of ocean memory and highlights how anomalies from some sectors may lead to divergent total Antarctic trends. Overall, although the paleo simulation is expected to better reproduce the present-day variability of the sea-ice extent than the instrumental simulation – due to a more physically consistent initialization – biases in the ocean–sea-ice model as well as in the atmospheric forcing may still introduce undesired behaviors, such as the 2003 sea-ice minimum that is not present in the instrumental simulation.

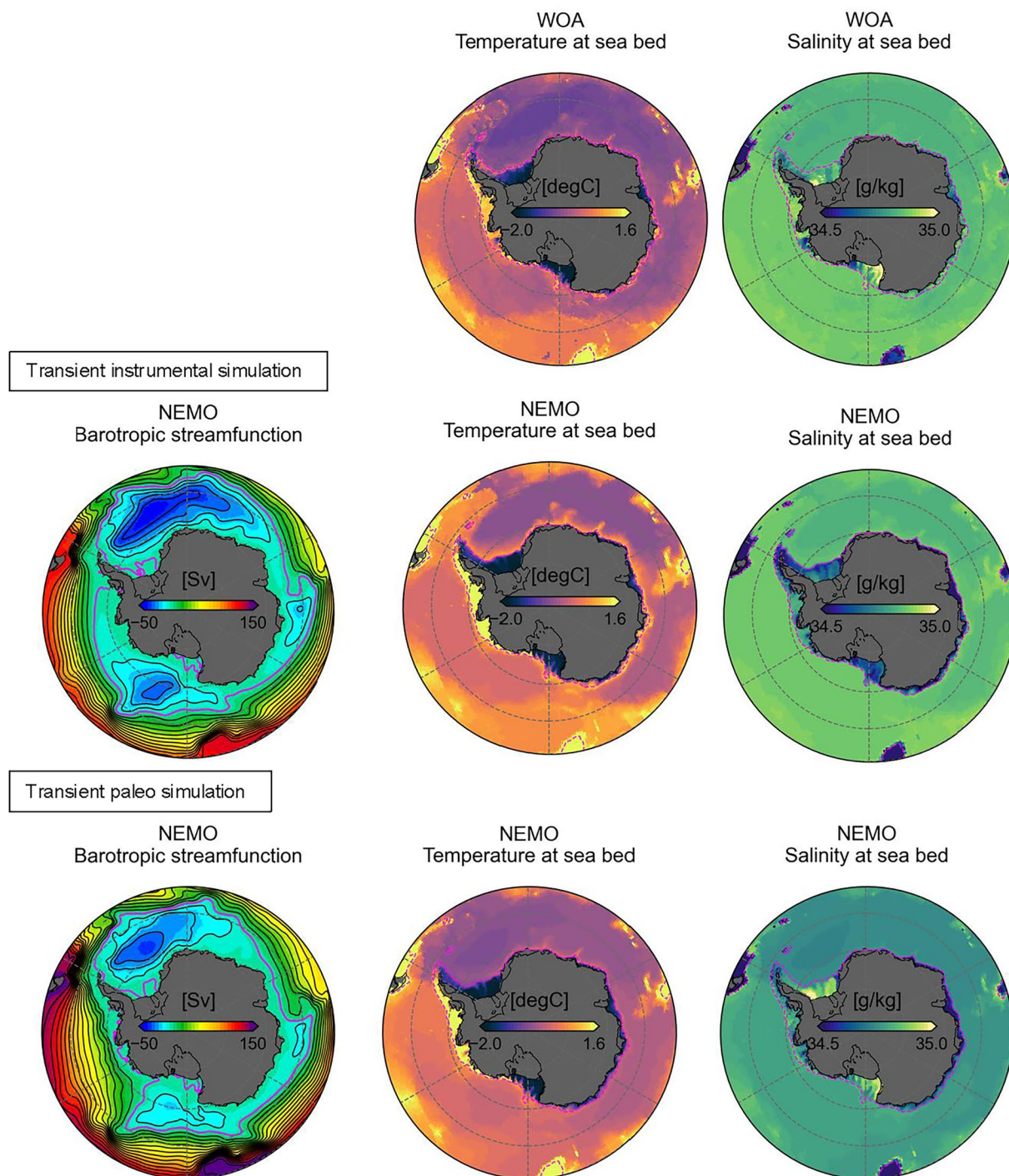


Fig. 5 (top) Annual salinity and temperature at the sea bed from WOA, averaged over 1981–2010. (middle and bottom) Annual barotropic stream function, salinity, and temperature at the sea bed from the transient instrumental and paleo simulations averaged over 1981–2010. The pink contour in the barotropic stream function corresponds to 0 Sv while the dashed pink contour for the salinity and temperature at the sea bed salinity represents the 1,200 m isoline.

Regarding the 20th century, compared to the reconstruction of Fogt *et al.*⁵⁷, both the atmospheric reanalysis and the transient paleo simulation indicate higher values for the total Antarctic sea-ice extent in the early 20th century (Fig. 8). Over 1905–1930, the difference with the Fogt *et al.*⁵⁷ reconstruction reaches $0.36 \times 10^6 \text{ km}^2$ for the atmospheric reanalysis and $0.82 \times 10^6 \text{ km}^2$ for the transient paleo simulation. The larger differences observed in the transient paleo simulation may reflect the influence of ocean memory responding to earlier atmospheric forcing, or the impact of remote oceanic changes – potentially driven by remote atmospheric variability. Investigating the origin of these discrepancies is key to improving our understanding of low-frequency

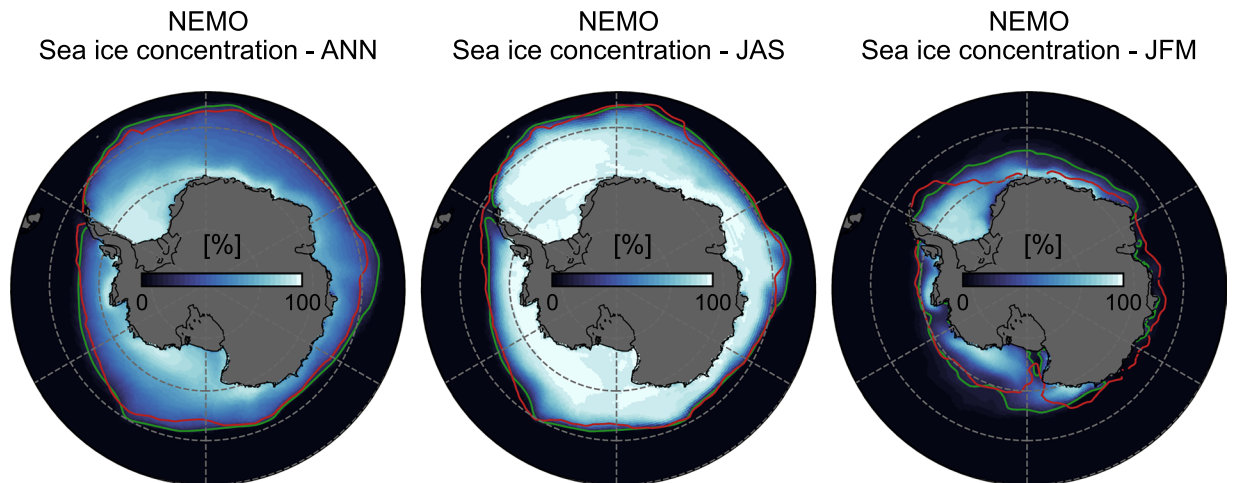
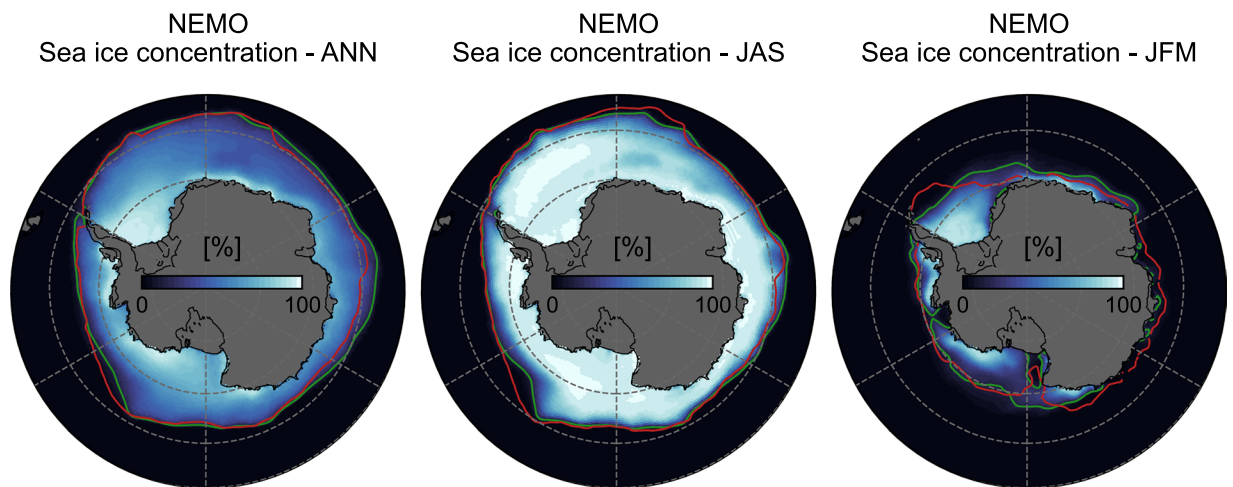
Transient instrumental run**Transient paleo run**

Fig. 6 Sea-ice concentration from the transient instrumental and paleo simulations averaged over 1981–2010 for the annual, winter, and summer means. The green line represents the simulated sea-ice edge (defined as the 15% concentration), while the red line indicates the corresponding edge derived from satellite-based observations (NSIDC G02202)³.

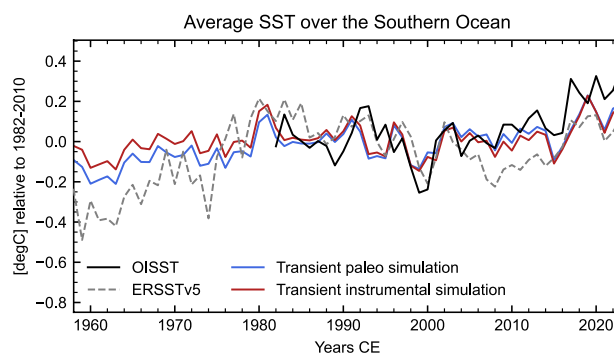


Fig. 7 Annual time series of sea surface temperature anomalies over the Southern Ocean (50°–60°South) based on OISST⁹⁴, ERSSTv5⁹⁵, transient instrumental and paleo simulations over 1958–2023. Anomalies are relative to the 1982–2010 period.

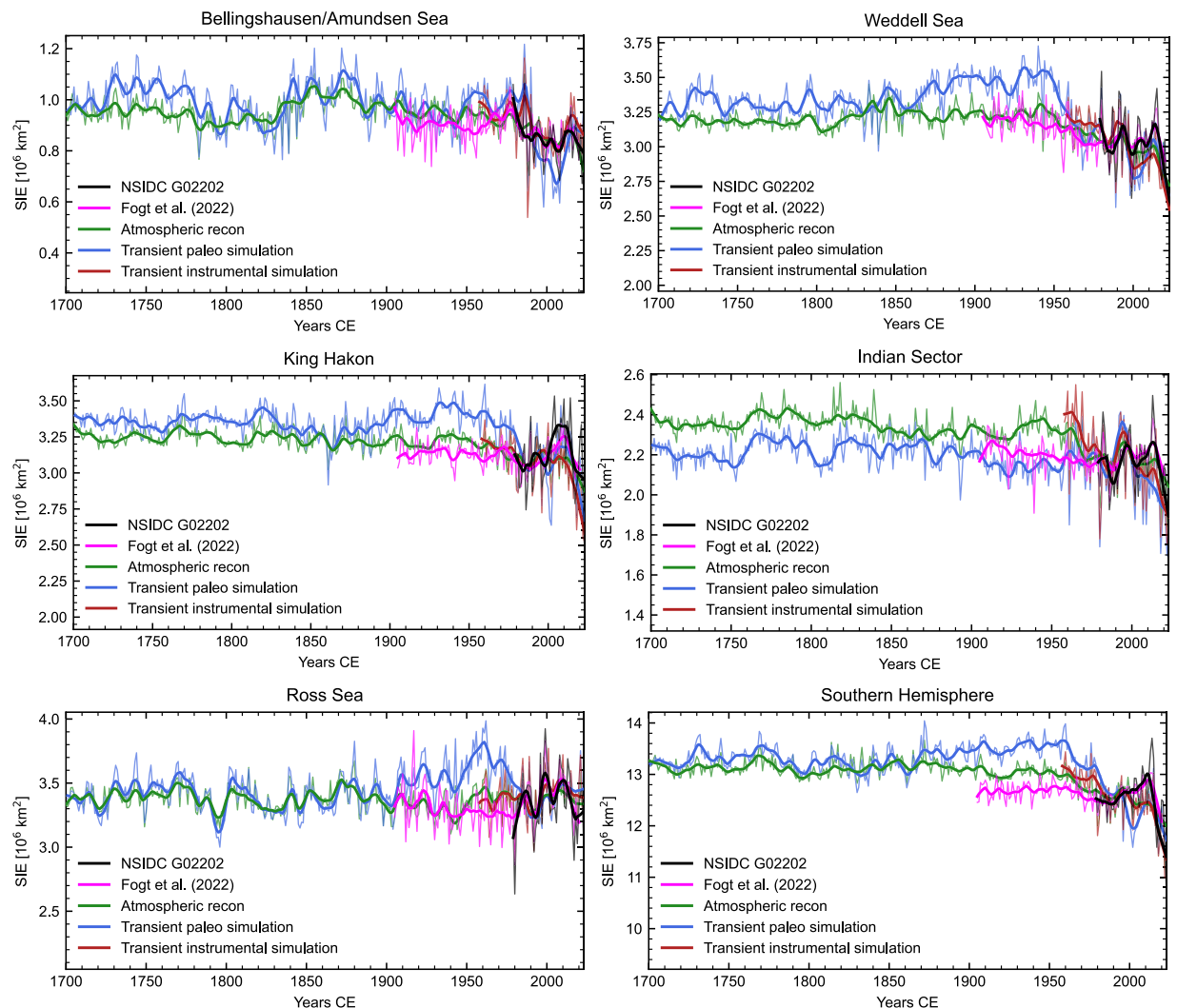


Fig. 8 Annual time series of regional sea-ice extent (10^6 km^2) for the five main Antarctic regions, as well as the total integrated extent for the Southern Hemisphere, based on observations (NSIDC G02202; black), the reconstruction of Fogt *et al.*⁵⁷ (magenta), the hybrid atmospheric reanalysis (atmospheric recon; green), the transient paleo simulation (blue), and the transient instrumental simulation (red) over 1700–2023. The thin lines represent the annual time-series while the thick lines are the 11-yr running averages. For the NEMO – SI³ simulations and the atmospheric reanalysis, the mean bias over 1981–2010 has been removed to match the observed 1981–2010 values. The five regions are defined as follows: the Amundsen/Bellingshausen Seas (110°W – 70°W), the Weddell Sea (70°W – 15°W), the King Hakon sector (15°W – 70°E), the Indian sector (70°E – 165°E), and the Ross Sea (165°E – 110°W).

and long-term sea-ice variability, particularly the role of oceanic processes. Furthermore, while our simulations suggest a more substantial sea-ice extent loss over the past century, the reconstruction by Fogt *et al.*⁵⁷ indicates relatively modest changes, with the most notable decline confined to the Weddell Sea. As highlighted by Goosse *et al.*⁴³, the lower sea-ice extent values over the 20th century in Fogt *et al.*⁵⁷ may be attributed to the reconstruction method relying on the atmospheric teleconnections, which could significantly underestimate the contribution of the ocean, as well as the non-inclusion of high-latitude observations, which primarily drive the long-term trends observed in the atmospheric reanalysis⁴³. The best agreement is found in the Weddell Sea, where observations from the Orcadas station are incorporated into all reconstructions, underlying the critical role of high-latitude observations in capturing the long-term trends.

The content of Methane Sulphonic Acid (MSA) in Antarctic ice cores has been widely used in previous studies (see Thomas *et al.*⁹⁷ for a review on paleoclimate proxies for sea-ice changes) to reconstruct past sea-ice conditions. The decline in sea-ice extent observed in the Bellingshausen/Amundsen Sea since around 1850 in both the transient paleo simulation and the atmospheric reconstruction aligns with the findings of Abram and Thomas⁹⁸, who used a MSA record from the Antarctic Peninsula to suggest a continuous retreat of the sea-ice edge since 1900. Similarly, based on a MSA ice core record from West Antarctica, Thomas *et al.*⁹⁹ reported a weak yet steady sea-ice expansion in the Ross Sea starting around 1940, superimposed by pronounced multi-decadal variability. The NEMO – SI³ simulations and the atmospheric reconstruction do not show statistically significant long-term

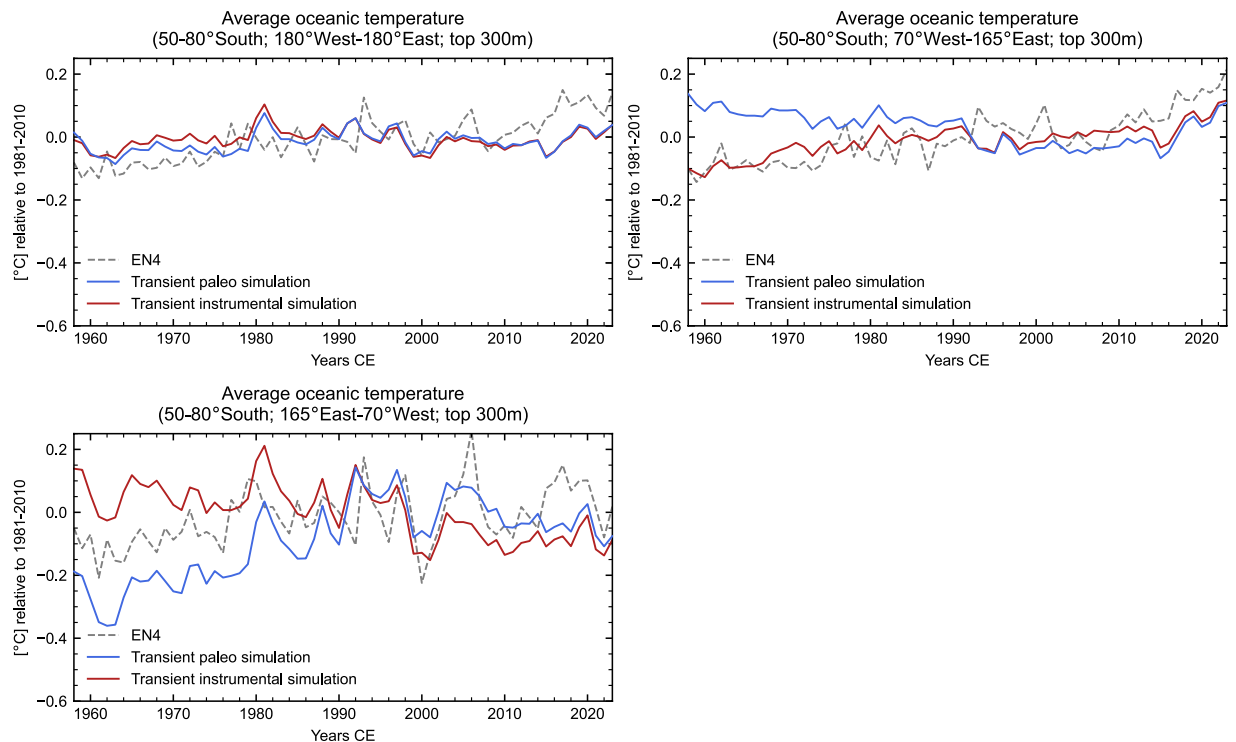


Fig. 9 Annual time series of mean oceanic temperature anomalies over the Southern Ocean (50°–80° South; upper 300 m; °C) from the transient paleo and instrumental simulation, and EN4 over 1958–2023. Anomalies are relative to the 1981–2010 period.

changes in this region but capture the multi-decadal variability. Besides, the transient paleo simulation displays a substantial sea-ice expansion in 1940–1970. The MSA record used in Thomas *et al.*⁹⁹ may reflect not only sea-ice changes but also changes in atmospheric circulation, as the onset of the observed sea-ice expansion coincides with a deepening of the Amundsen Sea Low^{29,100}, a persistent low-pressure system off the West Antarctic coast. In the Weddell Sea, the sea-ice decline over the 20th century captured by the NEMO – SI³ simulations and atmospheric reconstruction is consistent with observations of reduced landfast ice formation and shorter ice duration since the early 20th century¹⁰¹. Finally, German and Russian Antarctic Atlases suggest that the Southern Ocean in the early 20th century was covered by much more ice compared to the satellite period¹⁰². According to these sources, Antarctic sea-ice extent has declined by approximately 50% between the beginning of 20th century and present-day conditions. Although these atlases are associated with large uncertainties, the transient paleo simulation indicates a larger Antarctic sea-ice decline than both the transient instrumental simulation and the atmospheric reconstruction.

The transient paleo simulation displays a larger temporal variability compared with the atmospheric reanalysis (about two times larger when considering the total Southern Hemisphere over 1700–2023). Additionally, except for the Indian Sector, the transient paleo simulation displays a much larger sea-ice loss since 1950 compared with the atmospheric reanalysis (for the total Southern Hemisphere sea-ice extent, $-0.25 \times 10^6 \text{ km}^2 \text{ decade}^{-1}$ and $-0.13 \times 10^6 \text{ km}^2 \text{ decade}^{-1}$ for the transient paleo simulation and atmospheric reanalysis, respectively). In contrast with the atmospheric reanalysis, a sea-ice expansion is also noticed for the Weddell Sea over 1800–1950 and in Ross Seas over the early mid-20th century in the transient paleo simulation. Yet, a few studies^{32,103,104} indicate that these two regions display a large multi-decadal in the ocean variability, which ultimately impacts the sea-ice cover. Finally, differences between the transient paleo and instrumental simulations are also observed, with the transient paleo simulation exhibiting a greater overall sea-ice loss (a difference of $0.07 \times 10^6 \text{ km}^2$ in the total sea-ice extent trend over 1958–2023). Since the two simulations are driven by the same atmospheric forcing, the differences stem from the initial conditions, which have a greater influence at the beginning of the simulation but continue to be substantial at the end of the simulation. Stronger sea-ice extent trends are observed in the transient paleo simulation across all regions except for the Indian sector.

Historical oceanic temperature and circulation of the Southern Ocean since 1700. Evaluating subsurface ocean temperature in the Southern Ocean is much more challenging than assessing SST, primarily due to the limited availability of observations¹¹. Although gridded oceanic datasets are available, these products contain large uncertainties at high southern latitudes, especially beneath sea ice, where virtually no subsurface temperature profiles exist prior to the 1990s. As an initial assessment, we compare the annual mean ocean temperature integrated over the upper 300 meters from the two NEMO – SI³ simulations with the EN4 analysis¹⁰⁵, which is based on available subsurface observations, for the period 1958–2023 (Fig. 9). This comparison should not be considered a formal evaluation, as EN4 in the Southern Ocean largely relies on spatial interpolation from

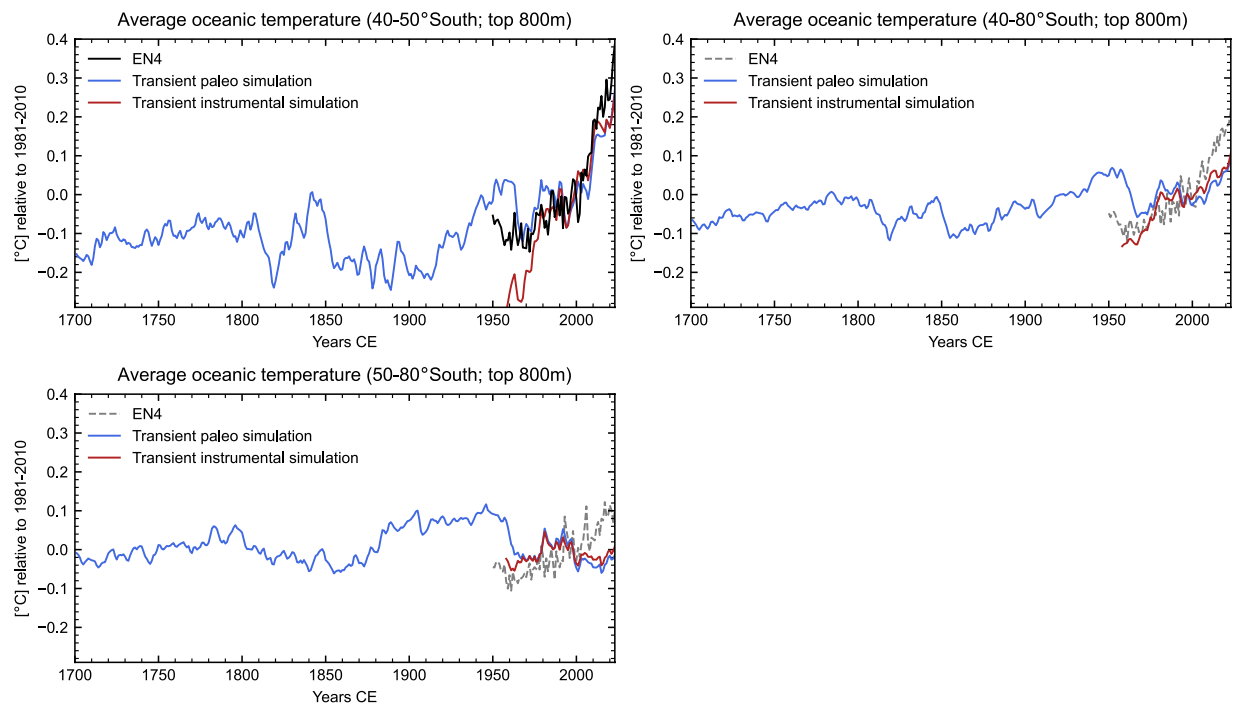


Fig. 10 Annual time series of mean oceanic temperature anomalies over 40°–50°South, 40°–80°South and 50°–80°South (upper 800m; °C) the transient paleo and instrumental simulations, and EN4 over 1700–2023. Anomalies are relative to the 1981–2010 period.

lower-latitude observations. Both simulations and EN4 reveal a warming phase from 1958 to the early 1990s, a relatively stable period afterwards, and then a subsequent warming. However, EN4 shows a larger amplitude of temperature change, consistent with SST trends from ERSSTv5 (which does not include observations from high southern latitudes before 1980). While the two simulations agree reasonably well when averaged over the entire Southern Ocean, substantial regional differences emerge (Fig. 9). Dividing the Southern Ocean into two sectors – West Antarctica (165°E–70°W) and East Antarctica (70°W–165°E) – reveals different behaviors: the transient paleo simulation shows cooling from 1958 to 2023 in the East Antarctic sector and warming in the West, while the transient instrumental simulation suggests the opposite. These contrasting results underscore the importance of model initialization in determining the simulated evolution of ocean temperatures.

To further assess the skill of the transient paleo simulation, we compute the annual ocean temperature over the upper 800 m of the Southern Ocean at mid-latitudes (Fig. 10), specifically between 40° and 50° South. Although this region is north of the Antarctic continent, it benefits from a higher density of observations and has exhibited a clear warming trend since the mid-20th century^{10,11}, making it a valuable region for evaluating the simulation. In addition to showing overall agreement with observations, the transient paleo simulation suggests that this warming trend may have begun in early 20th century. When extending the ocean heat content calculation to include high-latitude regions (40°–80° South), a significant discrepancy emerges: while EN4 indicates a steady warming trend since the mid-20th century, the transient paleo simulation instead suggests a more moderate warming with pronounced multi-decadal fluctuations. This disagreement becomes even more pronounced when focusing solely on the high-latitude region (50°–80° South), where EN4, like in other regions, depicts a strong warming trend, whereas the transient paleo simulation shows no clear trend since the 1950s. As previously noted, EN4 uncertainties are particularly large in this region, especially under sea ice.

We assess temperature variability over the Antarctic continental shelf ($\leq 1,200$ m) by integrating oceanic temperature between 200 and 700 m – a key proxy for ice shelf melt rates¹⁰⁶ – from the two NEMO – SI³ simulations (Fig. 11). Reliable, continent-wide observations of ice shelf melt rates have only been available since 1994^{23,107}, making it highly challenging to evaluate long-term variability. Except for the Western Atlantic sector, the two simulations exhibit significant differences in historical variability over 1958–2023. For Antarctica as a whole, the transient paleo simulation shows a warming trend of 0.033 °C decade⁻¹ (p-value < 0.001) over 1980–2023. However, as observed, this warming is regionally heterogeneous: while the sectors of Eastern Atlantic and Western Pacific show limited warming, the Western Pacific and Eastern Atlantic sectors (i.e., Amundsen, Bellingshausen, and Weddell Sea) have warmed significantly (on average, 0.053 °C decade⁻¹, statistically significant at the 99% confidence level). Albeit the average 200–700m oceanic temperature over the continental shelf does not correspond to the ice shelf melt rates, Naughten *et al.*¹⁰⁶ shows it is a relatively good proxy, at least for the Amundsen Sea. Therefore, the higher ice shelf melt rates observed over the past decades^{22–25} are coherent with the warmer ocean over the continental shelf.

Jacobs *et al.*¹⁰⁸ reported a freshening in the southwest Ross Sea that is not captured by the paleo simulation. This freshening is driven by the increased ice shelf melt in the Bellingshausen and Amundsen Seas, which is

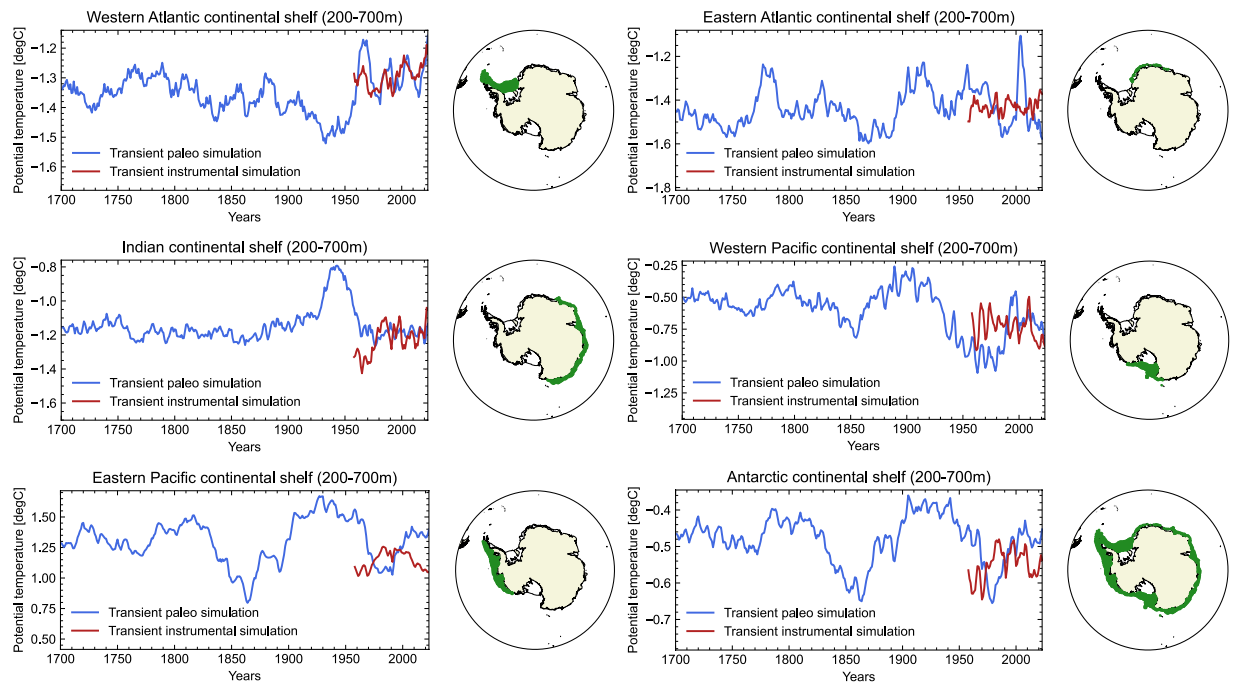


Fig. 11 Annual time-series of oceanic temperature (°C) averaged over 200–700m for the five main continental shelf regions of the Southern Ocean, along with the entire Southern Ocean from the transient instrumental and paleo simulations over 1700–2023. To ensure comparability, the mean over 1981–2010 has been removed from the transient instrumental simulation to align with the mean from the transient paleo simulation.

subsequently transported to the Ross Sea. The NEMO – SI³ configuration used in this study lacks the spatial resolution necessary to accurately represent ocean circulation within ice shelf cavities, and thus cannot simulate the meltwater contributions from these smaller ice shelves, thus explaining the discrepancy with the study of Jacobs *et al.*¹⁰⁸

Finally, Fig. S3 presents the anomalies of salinity vertical profiles for the five main regions of the Southern Ocean, along with the Southern Ocean as a whole, for both the transient paleo and instrumental simulations since 1700. In the Atlantic sector, the transient paleo simulation reveals a period of large salinity anomalies at mid-depth (200–400m) starting in the early 20th century, which reach the surface by the late 1960s. This triggers convection reaching depth of several hundreds of meters, which leads to the occurrence of large winter open-sea polynyas in the simulation. This bears interesting similarities with observations of large winter open-sea polynyas in the region during the 1970s (1974–1976; Weddell polynyas)¹⁰⁹. However, the simulated polynyas appear earlier than those observed in the 1970s. This timing mismatch may result from limitations in the atmospheric reanalysis used to drive the ocean model. In particular, the reconstruction method may overestimate atmospheric variability by attributing too much of the observed changes to atmospheric forcing, and not enough to ocean variability. Because the reconstruction does not account for coupled ocean-atmosphere feedback, it may artificially amplify atmospheric anomalies to match observed surface conditions. This could, in turn, prematurely trigger deep convection and the formation of open-ocean polynyas in the simulation.

Usage Notes

Our goal was to provide a coherent dataset for the atmosphere and ocean in Antarctica. This dataset is particularly designed for investigating low-frequency climate variability and for driving regional ocean–sea-ice and ice sheet models, to place observed changes over the past decades into a broader temporal context. This could ultimately reduce uncertainties regarding the contribution of the Antarctic Ice Sheet and its surroundings in the 21st future projections. Studying long-term climate variability in the high-latitude regions of the Southern Hemisphere remains challenging due to the sparse observational network and important biases in climate models – even during the satellite era. Despite efforts to minimize uncertainties in both the atmospheric and oceanic reconstructions, some degree of uncertainty is inherent due to limitations in, mainly here, paleoclimate records and the ocean–sea-ice model.

For the atmospheric reconstructions, we recommend users rely on the ensemble mean of the station-based reanalyses derived from different priors. This ensemble mean represents the the most robust estimate, as it smooths out individual ESM errors and extracts the common signal across reconstructions based on different ESMs. Since the paleo-based reanalysis is based on a unique prior, uncertainties related to the ESM used for reconstructing might be larger. However, the ESM used for the paleo-based reanalysis is CESM1, which has been intensively, and positively evaluated over the Antarctic region^{29,30,55,56}. In contrast with the station-based reanalysis, the number of assimilated records varies over time – increasing over time. As a result, the skill is higher in more recent periods where more records are available. To assess the reliability of the paleo-based reanalysis,

users should examine the ensemble spread, which provides a direct estimate of the constraint from the observations to the final reconstruction (reported as the standard deviation of the ensemble). A large spread indicates weak constraint from observations. Additionally, because the spatial and temporal distribution of proxy records is uneven, the skill of the reanalysis can vary significantly between regions. Users are therefore encouraged to assess uncertainty regionally and temporally depending on the focus of their analysis.

Regarding the ocean–sea-ice simulations, comparisons with available observations over recent decades indicate that the transient paleo simulation aligns more closely with observations than the transient instrumental simulation, which is initialized from present-day conditions. However, the transient paleo simulation exhibits notable biases over the East Antarctic sector. We argue that these biases are primarily due to the lower skill of the paleo-based atmospheric reanalysis in East Antarctica compared to West Antarctica. As such, for applications focused on East Antarctica, we strongly advise users to carefully evaluate the behavior of the simulation in this region.

In addition, the transient paleo simulation displays pronounced multi-decadal variability, particularly at the regional scale. Importantly, this large variability is not constrained by oceanic observations, and substantial temperature anomalies seen in some regions are not yet fully understood. While the transient paleo simulation provides physically consistent responses to the reconstructed atmospheric forcing, it should be viewed as an uncertain historical realization rather than a validated reconstruction of past ocean conditions. However, although the reliability of this low-frequency variability is difficult to assess – mainly due to the scarcity of observations – there are studies considering discrepancy between ESM simulations and paleoclimate records in this regard³⁸. ESMs tend to simulate much weaker low-frequency variability than is inferred from paleoclimate records. The enhanced multi-decadal variability seen in the transient paleo simulation therefore may be in better agreement with paleoclimate evidence. Nevertheless, this strong low-frequency variability is a key characteristic of the dataset and could pose challenges for certain applications – especially for ocean–sea-ice or ice sheet models calibrated using only the instrumental period, which may not capture the full range of natural variability. In such cases, we recommend that users assess the amplitude of low-frequency variability in their region of interest to ensure compatibility with their model framework. For users primarily interested in pre-industrial conditions and seeking to minimize the potential issues related to the low-frequency variability, we recommend averaging the transient paleo simulation over a period prior to 1950 to derive a representative estimate of the pre-industrial climate state. Additionally, users may find it valuable to compare the transient instrumental and paleo simulations. The transient paleo simulation likely better captures low-frequency variability due to a more realistic representation of oceanic circulation, but it may also be more susceptible to model biases³⁶. In contrast, the transient instrumental simulation is expected to more closely resemble the observed present-day state, yet it may significantly underestimate historical oceanic changes, especially at depth.

Finally, this dataset is based on a coarse spatial resolution (i.e., 1°) for both the atmosphere and ocean, and is therefore primarily designed to capture large-scale features. Caution is advised when using it to study local processes. For such applications, we recommend first assessing the performance of the reconstruction at the zone of interest and, if needed, applying a downscaling method – either statistical or dynamical (e.g., using a regional ocean–sea-ice model) – to enhance spatial resolution and to reduce these biases. Future versions of this dataset will aim to:

1. implement a method to improve the consistency between atmospheric and oceanic reanalyses by producing a fully coupled atmosphere–ocean reanalysis over the past centuries¹⁰;
2. apply a statistical downscaling technique to increase the spatial variability in the atmospheric reanalysis¹¹¹;
3. use a higher-resolution configuration of NEMO – SI³ to explicitly resolve ocean circulation within all the Antarctic ice shelf cavities⁷⁰.

Code availability

The code for performing the atmospheric reanalysis can be found on Github (https://github.com/dalaiden/DA_offline_PF). The code used for the NEMO – SI³ simulations is publicly available by the NEMO consortium (<https://www.nemo-ocean.eu/>) and is distributed under the CeCILL license (http://cecill.info/licences/Licence_CeCILL_V2-en.txt). All the data generated in the study are archived on Zenodo (<https://doi.org/10.5281/zenodo.15472051>).

Received: 17 June 2025; Accepted: 11 August 2025;

Published online: 26 September 2025

References

1. IPCC. IPCC Special Report on the Ocean and Cryosphere in a Changing Climate [H.-O. Pörtner, D.C. Roberts, V. Masson-Delmotte, P. Zhai, M. Tignor, E. Poloczanska, K. Mintenbeck, A. Alegria, M. Nicolai, A. Okem, J. Petzold, B. Rama, N.M. Weyer (eds.)]. *In press*, (2019).
2. Bromwich, D. H. *et al.* Central West Antarctica among the most rapidly warming regions on Earth. *Nature Geoscience* **6**(2), 139–145 (2013).
3. Parkinson, C. L. A 40-y record reveals gradual Antarctic sea ice increases followed by decreases at rates far exceeding the rates seen in the Arctic. *Proceedings of the National Academy of Sciences of the United States of America* **116**(29), 14414–14423 (2019).
4. Purich, A. & Doddridge, E. W. Record low Antarctic sea ice coverage indicates a new sea ice state. *Communications Earth and Environment* **4**(1), 1–9 (2023).
5. Marshall, G. J. & Thompson, David W. J. The signatures of large-scale patterns of atmospheric variability in Antarctic surface temperatures. *Journal of Geophysical Research* **121**(7), 3276–3289 (2016).
6. Marshall, G. J., Thompson, David W. J. & van den Broeke, M. R. The Signature of Southern Hemisphere Atmospheric Circulation Patterns in Antarctic Precipitation. *Geophysical Research Letters* **44**(22), 11,580–11,589 (2017).

7. Medley, B. & Thomas, E. R. Increased snowfall over the Antarctic Ice Sheet mitigated twentieth-century sea-level rise. *Nature Climate Change* **9**(1), 34–39 (2019).
8. Fogt, R. L. & Marshall, G. J. The Southern Annular Mode: Variability, trends, and climate impacts across the Southern Hemisphere. *WIREs Climate Change* **n/a**(n/a), e652 (2020).
9. Hobbs, W. *et al.* Observational evidence for a regime shift in summer antarctic sea ice. *Journal of Climate* (2024).
10. Swart, N. C., Gille, S. T., Fyfe, J. C. & Gillett, N. P. Recent Southern Ocean warming and freshening driven by greenhouse gas emissions and ozone depletion. *Nature Geoscience* **11**(11), 836–841 (2018).
11. Hobbs, W. R., Roach, C., Roy, T., Sallée, Jean-Baptiste & Bindoff, N. Anthropogenic temperature and salinity changes in the southern ocean. *Journal of Climate* **34**(1), 215–228 (2021).
12. Josey, S. A. *et al.* Record-low Antarctic sea ice in 2023 increased ocean heat loss and storms. *Nature* **636**(8043), 635–639 (2024).
13. Medley, B. *et al.* Temperature and Snowfall in Western Queen Maud Land Increasing Faster Than Climate Model Projections. *Geophysical Research Letters* **45**(3), 1472–1480 (2018).
14. Lenaerts, J. T. M. *et al.* Recent snowfall anomalies in Dronning Maud Land, East Antarctica, in a historical and future climate perspective. *Geophysical Research Letters* **40**(11), 2684–2688 (2013).
15. Schlosser, E. *et al.* Recent climate tendencies on an East Antarctic ice shelf inferred from a shallow firn core network. *Journal of Geophysical Research Atmospheres* **119**, 6578–6595 (2014).
16. Altnau, S., Schlosser, E., Isaksson, E. & Divine, E. Climatic signals from 76 shallow firn cores in Dronning Maud Land, East Antarctica. *Cryosphere* **9**(3), 925–944 (2015).
17. Wauthy, S. *et al.* Spatial and temporal variability of environmental proxies from the top 120m of two ice cores in dronning maud land (east antarctica). *Earth System Science Data* **16**(1), 35–58 (2024).
18. Wang, D. *et al.* Sustained decrease in inland East Antarctic surface mass balance between 2005 and 2020. *Nature Geoscience* **18**(6), 462–470 (2025).
19. Rignot, E., Jacobs, S., Mouginot, J. & Scheuchl, B. Ice-shelf melting around antarctica. *Science* **341**(6143), 266–270 (2013).
20. Mouginot, J., Rignot, E. & Scheuchl, B. Sustained increase in ice discharge from the amundsen sea embayment, west antarctica, from 1973 to 2013. *Geophysical Research Letters* **41**(5), 1576–1584 (2014).
21. Smith, J. A. *et al.* Sub-ice-shelf sediments record history of twentieth-century retreat of Pine Island Glacier. *Nature* **541**(7635), 77–80 (2017).
22. Pritchard, H. D. *et al.* Antarctic ice-sheet loss driven by basal melting of ice shelves. *Nature* **484**(7395), 502–505 (2012).
23. Adusumilli, S., Fricker, H. A., Medley, B., Padman, L. & Siegfried, M. R. Interannual variations in meltwater input to the Southern Ocean from Antarctic ice shelves. *Nature Geoscience* **13**(9), 616–620 (2020).
24. Smith, B. *et al.* Pervasive ice sheet mass loss reflects competing ocean and atmosphere processes. *Science*, **5845**(April) 1–13, (2020).
25. Otosaka, I. N. *et al.* Mass balance of the greenland and antarctic ice sheets from 1992 to 2020. *Earth System Science Data* **15**(4), 1597–1616 (2023).
26. Jones, J. M. *et al.* Assessing recent trends in high-latitude Southern Hemisphere surface climate. *Nature Climate Change* **6**(10), 917–926 (2016).
27. Barthel, A. *et al.* Cmp5 model selection for ismip6 ice sheet model forcing: Greenland and antarctica. *The Cryosphere* **14**(3), 855–879 (2020).
28. Roach, L. A., Eisenman, I., Wagner, T. J., Blanchard-Wrigglesworth, E. & Bitz, C. M. Asymmetry in the seasonal cycle of antarctic sea ice due to insolation. *Nat. Geosci.* **15**(4), 277–281 (2022).
29. Dalaiden, Q., Goosse, H., Rezsöházy, J. & Thomas, E. R. Reconstructing atmospheric circulation and sea-ice extent in the west antarctic over the past 200 years using data assimilation. *Climate Dynamics* **57**(11), 3479–3503 (2021).
30. O'Connor, G. K., Steig, E. J. & Hakim, G. J. Strengthening Southern Hemisphere Westerlies and Amundsen Sea Low Deepening Over the 20th Century Revealed by Proxy–Data Assimilation. *Geophysical Research Letters* **48**(24), (2021).
31. Dalaiden, Q., Rezsöházy, J. *et al.* An unprecedented sea ice retreat in the weddell sea driving an overall decrease of the antarctic sea-ice extent over the 20th century. *Geophysical Research Letters* **50**(21), e2023GL104666 (2023).
32. Crosta, X. *et al.* Multi-decadal trends in Antarctic sea-ice extent driven by ENSO–SAM over the last 2,000 years. *Nature Geoscience* **14**(3), 156–160 (2021).
33. Fox-Kemper, B. *et al.* Ocean, cryosphere and sea level change. Ocean, Cryosphere and Sea Level Change, in: *Climate Change 2021: The Physical Science Basis. Contribution of Working Group I to the Sixth Assessment Report of the Intergovernmental Panel on Climate Change*, (2021).
34. Edwards, T. L. *et al.* Projected land ice contributions to twenty-first-century sea level rise. *Nature* **593**(7857), 74–82 (2021).
35. Seroussi, H. *et al.* Insights into the vulnerability of antarctic glaciers from the ismip6 ice sheet model ensemble and associated uncertainty. *The Cryosphere* **17**(12), 5197–5217 (2023).
36. Cailliet, J. *et al.* Uncertainty in the projected antarctic contribution to sea level due to internal climate variability. *Earth System Dynamics* **16**(1), 293–315 (2025).
37. Casado, M., Hébert, R., Faranda, D. & Landais, A. The quandary of detecting the signature of climate change in Antarctica. *Nature Climate Change* **13**(10), 1082–1088 (2023).
38. Laepple, T. *et al.* Regional but not global temperature variability underestimated by climate models at supradecadal timescales. *Nature Geoscience* **16**(11), 958–966 (2023).
39. Hakim, G. J. *et al.* The last millennium climate reanalysis project: Framework and first results. *Journal of Geophysical Research* **121**(12), 6745–6764 (2016).
40. Steiger, N. J., Smerdon, J. E., Cook, E. R. & Cook, B. I. A reconstruction of global hydroclimate and dynamical variables over the Common Era. *Scientific Data* **5**, 1–15 (2018).
41. Valler, V. *et al.* ModE-RA: a global monthly paleo-reanalysis of the modern era 1421 to 2008. *Scientific Data* **11**(1), 1–19 (2024).
42. Turner, J. The El Niño–Southern Oscillation and Antarctica. *International Journal of Climatology* **24**(1), 1–31 (2004).
43. Goosse, H., Dalaiden, Q., Mezzina, B. & Fogt, R. L. A drop in Antarctic sea ice extent at the end of the 1970s. *Communications Earth & Environment* (2024).
44. Brady, E. *et al.* The Connected Isotopic Water Cycle in the Community Earth System Model Version 1. *Journal of Advances in Modeling Earth Systems* **11**(8), 2547–2566 (2019).
45. Stevenson, S., Capotondi, A., Fasullo, J. & Otto-Bliesner, B. Forced changes to twentieth century ENSO diversity in a last Millennium context. *Climate Dynamics* **52**(12), 7359–7374 (2019).
46. Danabasoglu, G. *et al.* North atlantic simulations in coordinated ocean-ice reference experiments phase ii (core-ii). part i: Mean states. *Ocean Modelling* **73**, 76–107 (2014).
47. Hutchinson, K. *et al.* Improving Antarctic Bottom Water precursors in NEMO for climate applications. *Geoscientific Model Development* **16**(12), 3629–3650 (2023).
48. van Leeuwen, P. J. Particle Filtering in Geophysical Systems. *Monthly Weather Review* **137**(12), 4089–4114 (2009).
49. Dubinkina, S., Goosse, H., Sallaz-Damaz, Y., Crespin, E. & Crucifix, M. Testing a Particle Filter To Reconstruct Climate Changes Over the Past Centuries. *International Journal of Bifurcation and Chaos* **21**(12), 3611–3618 (2011).
50. Klein *et al.* Assessing the robustness of Antarctic temperature reconstructions over the past two millennia using pseudoproxy and data assimilation experiments. *Climate of the Past* **15**, 661–684 (2019).

51. Rezsöhazy, J., Dalaiden, Q., Klein, F., Goosse, H. & Guiot, J. Using a process-based dendroclimatic proxy system model in a data assimilation framework: a test case in the southern hemisphere over the past centuries. *Climate of the Past* **18**(9), 2093–2115 (2022).
52. Goosse, H. Reconstructed and simulated temperature asymmetry between continents in both hemispheres over the last centuries. *Climate Dynamics* **48**(5–6), 1483–1501 (2017).
53. Matsikaris, A., Widmann, M. & Jungclaus, J. On-line and off-line data assimilation in palaeoclimatology: A case study. *Climate of the Past* **11**(1), 81–93 (2015).
54. Oger, S., Sime, L. & Holloway, M. Decoupling of $\delta^{18}\text{O}$ from surface temperature in antarctica in an ensemble of historical simulations. *EGU sphere* **2023**, 1–29 (2023).
55. Agosta, C., Fettweis, X. & Datta, R. Evaluation of the CMIP5 models in the aim of regional modelling of the Antarctic surface mass balance. *The cryosphere* **9**, 2311–2032 (2015).
56. Lenaerts, J. T. M., Vizcaino, M., Fyke, J., van Kampenhout, L. & van den Broeke, M. R. Present-day and future Antarctic ice sheet climate and surface mass balance in the Community Earth System Model. *Climate Dynamics* **47**(5–6), 1367–1381 (2016).
57. Fogt, R. L., Sleinkofer, A. M., Raphael, M. N. & Handcock, M. S. A regime shift in seasonal total Antarctic sea ice extent in the twentieth century. *Nature Climate Change* **12**(1), 54–62 (2022).
58. Dalaiden, Q. *et al.* Reconstructed sea ice and winds [Dataset], (2023).
59. Stenni, B. *et al.* Antarctic climate variability on regional and continental scales over the last 2000 years. *Climate of the Past* **13**(11), 1609–1634 (2017).
60. Stenni, B. *et al.* Regional Antarctic snow accumulation over the past 1000 years [Dataset], 2017. last access: 17 April (2020).
61. Thomas, E. R. *et al.* Regional Antarctic snow accumulation over the past 1000 years. *Climate of the Past* **13**(11), 1491–1513 (2017).
62. Thomas, E. R. *et al.* Dixon, Massimo Frezzotti, Barbara Stenni, Mark Curran, and Alexey A. Ekaykin. Regional Antarctic snow accumulation over the past 1000 years [Dataset], 2017. last access: 17 April (2020).
63. Thomas, E. R. *et al.* Ice core chemistry database: an antarctic compilation of sodium and sulphate records spanning the past 2000 years. *Earth System Science Data Discussions* **2022**, 1–20 (2022).
64. Thomas, E. R. *et al.* Ice core chemistry database: an Antarctic compilation of sodium and sulphate records spanning the past 2000 years [Dataset], 2017. last access: 3 February (2022).
65. Evans, M. N., Tolwinski-Ward, S. E., Thompson, D. M. & Anchukaitis, K. J. Applications of proxy system modeling in high resolution paleoclimatology. *Quaternary Science Reviews* **76**, 16–28 (2013).
66. Oke, P. R. & Sakov, P. Representation error of oceanic observations for data assimilation. *Journal of Atmospheric and Oceanic Technology* **25**(6), 1004–1017 (2008).
67. Janjić, T. *et al.* On the representation error in data assimilation. *Quarterly Journal of the Royal Meteorological Society* **144**(713), 1257–1278 (2018).
68. Tardif, R. *et al.* Last millennium reanalysis with an expanded proxy database and seasonal proxy modeling. *Climate of the Past* **15**(4), 1251–1273 (2019).
69. NEMO System Team. Nemo ocean engine, March (2022).
70. Mathiot, P., Jenkins, A., Harris, C. & Madec, G. Explicit and parametrised representation of under ice shelf seas in a z^* coordinate ocean model. *Geoscientific Model Development* **10**, 2849–2874 (2017).
71. NOAA. National Geophysical Data Center 2-minute gridded global relief data (ETOPO2) v2, (2006).
72. Arndt, J. E. *et al.* The international bathymetric chart of the Southern Ocean (IBCSO) version 1.0-A new bathymetric compilation covering circum-Antarctic waters. *Geophysical Research Letters* **40**(12), 3111–3117 (2013).
73. Rousset, C. *et al.* The Louvain-La-Neuve sea ice model LIM3.6: Global and regional capabilities. *Geoscientific Model Development* **8**(10), 2991–3005 (2015).
74. Vancoppenolle, M. *et al.* Si3, the nemo sea ice engine, January (2023).
75. Locarnini, R. A. *et al.* World ocean atlas 2013. Volume 1, Temperature, (2013).
76. Zweng, M. M. *et al.* World ocean atlas 2013. Volume 2, Salinity, (2013).
77. Depoorter, M. A. *et al.* Calving fluxes and basal melt rates of Antarctic ice shelves. *Nature*, 502, 89–92, <https://doi.org/10.1038/nature12567> (2013).
78. Hersbach, H. *et al.* The ERA5 global reanalysis. *Quarterly Journal of the Royal Meteorological Society* **146**(730), 1999–2049 (2020).
79. Naughten, K. A. *et al.* Intercomparison of Antarctic ice-shelf, ocean, and sea-ice interactions simulated by MetROMS-iceshelf and FESOM 1.4. *Geoscientific Model Development* **11**(4), 1257–1292 (2018).
80. Dalaiden, Q. Dynamical reconstruction of southern ocean and antarctic climate variability since 1700. *Zenodo*. <https://doi.org/10.5281/zenodo.15472051> (2025).
81. Caton Harrison, T. *et al.* Reanalysis representation of low-level winds in the Antarctic near-coastal region. *Weather and Climate Dynamics* **3**(4), 1415–1437 (2022).
82. Gossart, A. *et al.* An Evaluation of Surface Climatology in State-of-the-Art Reanalyses over the Antarctic Ice Sheet. *Journal of Climate* **32**(20), 6899–6915 (2019).
83. Marshall, G. J. Trends in the Southern Annular Mode from Observations and Reanalyses. *Journal of Climate* **16**(1999), 4134–4143 (2003).
84. van Wessem, J. M. *et al.* Modelling the climate and surface mass balance of polar ice sheets using RACMO2, part 2: Antarctica (1979–2016). *The Cryosphere* **12**, 1479–1498 (2018).
85. Bromwich, D. H., Ensign, A., Wang, S. H. & Zou, X. Major Artifacts in ERA5 2-m Air Temperature Trends Over Antarctica Prior to and During the Modern Satellite Era. *Geophysical Research Letters*, **51**(21), (2024).
86. Eswaran, A., Truax, O. J. & Fudge, T. J. 20th-Century Antarctic Sea Level Mitigation Driven by Uncertain East Antarctic Accumulation History. *Geophysical Research Letters*, **51**(9), (2024).
87. Orsi, A. H., Whitworth, T. & Nowlin, W. D. On the meridional extent and fronts of the Antarctic Circumpolar Current. *Deep-Sea Research Part I* **42**(5), 641–673 (1995).
88. Holland, P. R. *et al.* Modeled trends in antarctic sea ice thickness. *Journal of Climate* **27**(10), 3784–3801 (2014).
89. Cunningham, S. A., Alderson, S. G., King, B. A. & Brandon, M. A. Transport and variability of the Antarctic Circumpolar Current in Drake Passage. *Journal of Geophysical Research: Oceans*, **108**(C5) (2003).
90. Donohue, K. A., Tracey, K. L., Watts, D. R., Chidichimo, M. P. & Chereskin, T. K. Mean Antarctic Circumpolar Current transport measured in Drake Passage. *Geophysical Research Letters* **43**(22), 11,760–11,767 (2016).
91. Mazloff, M. R., Heimbach, P. & Wunsch, C. An eddy-permitting Southern Ocean state estimate. *Journal of Physical Oceanography* **40**(5), 880–899 (2010).
92. Lellouche, Jean-Michel *et al.* The Copernicus Global 1/12° Oceanic and Sea Ice GLORYS12 Reanalysis. *Frontiers in Earth Science*, **9** (2021).
93. Mathiot, P. & Jourdain, N. C. Southern Ocean warming and Antarctic ice shelf melting in conditions plausible by late 23rd century in a high-end scenario. *Ocean Science* **19**(6), 1595–1615 (2023).
94. Huang, B. *et al.* Improvements of the Daily Optimum Interpolation Sea Surface Temperature (DOISST) Version 2.1. *Journal of Climate* **34**(8), 2923–2939 (2021).
95. Huang, B. *et al.* Extended Reconstructed Sea Surface Temperature, Version 5 (ERSSTv5): Upgrades, Validations, and Intercomparisons. *Journal of Climate* **30**(20), 8179–8205 (2017).

96. NSIDC. Satellite sea-ice concentration product [Dataset] (2023). last access on June 20, (2022).
97. Thomas, E. R. *et al.* Antarctic Sea Ice Proxies from Marine and Ice Core Archives Suitable for Reconstructing Sea Ice over the past 2000 Years. *Geosciences*, pages 1–33, (2019).
98. Abram, N. J. *et al.* Ice core evidence for a 20th century decline of sea ice in the Bellingshausen Sea, Antarctica. *Journal of Geophysical Research Atmospheres* **115**(23), 1–9 (2010).
99. Thomas, E. R. & Abram, N. J. Ice core reconstruction of sea ice change in the Amundsen-Ross Seas since 1702 A.D. *Geophysical Research Letters* **43**(10), 5309–5317 (2016).
100. O'Connor, G. K., Holland, P. R., Steig, E. J., Dutrieux, P. & Hakim, G. J. Characteristics and rarity of the strong 1940s westerly wind event over the amundsen sea, west antarctica. *The Cryosphere* **17**(10), 4399–4420 (2023).
101. Murphy, E. J., Clarke, A., Abram, N. J. & Turner, J. Variability of sea-ice in the northern weddell sea during the 20th century. *Journal of Geophysical Research: Oceans* **119**(7), 4549–4572 (2014).
102. Titchner, H. A. & Rayner, N. A. The met office hadley centre sea ice and sea surface temperature data set, version 2: 1. sea ice concentrations. *Journal of Geophysical Research: Atmospheres* **119**(6), 2864–2889 (2014).
103. Zhang, X., Deser, C. & Sun, L. Is there a tropical response to recent observed southern ocean cooling? *Geophysical Research Letters* **48**(5), e2020GL091235 (2021).
104. Morioka, Y. *et al.* Multidecadal variability and predictability of antarctic sea ice in the gfdl spear_lo model. *The Cryosphere* **17**(12), 5219–5240 (2023).
105. Good, S. A., Martin, M. J. & Rayner, N. A. En4: Quality controlled ocean temperature and salinity profiles and monthly objective analyses with uncertainty estimates. *Journal of Geophysical Research: Oceans* **118**(12), 6704–6716 (2013).
106. Naughten, K. A. *et al.* Simulated Twentieth-Century Ocean Warming in the Amundsen Sea, West Antarctica. *Geophysical Research Letters*, **49**(5), (2022).
107. Paolo, F. S., Fricker, H. A. & Padman, L. Volume loss from Antarctic ice shelves is accelerating. *Science* **348**(6232), 327–331 (2015).
108. Jacobs, S. S., Giulivi, C. F. & Dutrieux, P. Persistent ross sea freshening from imbalance west antarctic ice shelf melting. *Journal of Geophysical Research: Oceans* **127**(3), e2021JC017808 (2022).
109. Comiso, J. C. & Gordon, A. L. Recurring polynyas over the cosmonaut sea and the maud rise. *Journal of Geophysical Research: Oceans* **92**(C3), 2819–2833 (1987).
110. Laloyaux, P., Balmaseda, M., Dee, D., Mogensen, K. & Janssen, P. A coupled data assimilation system for climate reanalysis. *Quarterly Journal of the Royal Meteorological Society* **142**(694), 65–78 (2016).
111. Barthélémy, S., Brajard, J., Bertino, L. & Counillon, F. Super-resolution data assimilation. *Ocean Dynamics* **72**(8), 661–678 (2022).
112. Rashid, H. A. *et al.* Evaluation of climate variability and change in ACCESS historical simulations for CMIP6. *Journal of Southern Hemisphere Earth Systems Science* **72**(2), 73–92 (2022).
113. Kirchmeier-Young, M. C., Zwiers, F. W. & Gillett, N. P. Attribution of extreme events in Arctic Sea ice extent. *Journal of Climate* **30**(2), 553–571 (2017).
114. Swart, N. C. *et al.* The canadian earth system model version 5 (canesm5.0.3). *Geoscientific Model Development* **12**(11), 4823–4873 (2019).
115. Otto-Bliesner, B. L. *et al.* Climate Variability and Change since 850 CE: An Ensemble Approach with the Community Earth System Model. *Bulletin of the American Meteorological Society* **97**(5), 735–754 (2015).
116. Rodgers, K. B. *et al.* Ubiquity of human-induced changes in climate variability. *Earth System Dynamics* **12**(4), 1393–1411 (2021).
117. Voldoire, A. *et al.* Evaluation of cmip6 deck experiments with cnrm-cm6-1. *Journal of Advances in Modeling Earth Systems* **11**(7), 2177–2213 (2019).
118. Boucher, O. *et al.* Presentation and evaluation of the ipsl-cm6a-lr climate model. *Journal of Advances in Modeling Earth Systems* **12**(7), e2019MS002010 (2020).
119. Maher, N. *et al.* The max planck institute grand ensemble: Enabling the exploration of climate system variability. *Journal of Advances in Modeling Earth Systems* **11**(7), 2050–2069 (2019).
120. Bethke, I. *et al.* Norcpm1 and its contribution to cmip6 dcpp. *Geoscientific Model Development* **14**(11), 7073–7116 (2021).
121. Sellar, A. A. *et al.* Ukesm1: Description and evaluation of the u.k. earth system model. *Journal of Advances in Modeling Earth Systems* **11**(12), 4513–4558 (2019).
122. Steig, E. J. *et al.* Warming of the Antarctic ice-sheet surface since the 1957 International Geophysical Year. *Nature* **457**(7228), 459–462 (2009).

Acknowledgements

This project has received funding from the Fond de la Recherche Scientifique de Belgique (F.R.S.-FNRS; Belgium) and European Union's Horizon 2020 research and innovation programme under the Marie Skłodowska-Curie grant agreement 101149188. Computational resources have been provided by the supercomputing facilities of the Université catholique de Louvain (CISM/UCL) and the Consortium des Équipements de Calcul Intensif en Fédération Wallonie Bruxelles (CÉCI) funded by the F.R.S.-FNRS under convention 2.5020.11 and by the Walloon Region. The present research benefited from computational resources made available on Lucia, the Tier-1 supercomputer of the Walloon Region, infrastructure funded by the Walloon Region under the grant agreement n°1910247. We would first like to thank Katherine Hutchinson for archiving the NEMO – SI³ eORCA1 configuration used in this study. We are also grateful to Pierre-Yves Barriat for his technical assistance with supercomputer usage. We thank Kaitlin Naughten for helpful discussions on the creation of high-frequency atmospheric forcing for ocean model simulations. Justine Caillet is thanked for her feedback on an earlier version of the manuscript. Finally, this work would not have been possible without the publicly available instrumental and proxy records, as well as model outputs from international modelling groups. We sincerely thank both communities for their contributions.

Author contributions

Q.D. designed the study through numerous discussions with H.G. and P.R.H. Q.D. conducted the experiments, generated the figures, analyzed the results, and wrote the initial draft of the manuscript. A.B. developed the framework around NEMO – SI³ (i.e., launcher). All authors contributed to the discussion of the results and the final version of the manuscript.

Competing interests

The authors declare no competing interests.

Additional information

Supplementary information The online version contains supplementary material available at <https://doi.org/10.1038/s41597-025-05808-w>.

Correspondence and requests for materials should be addressed to Q.D.

Reprints and permissions information is available at www.nature.com/reprints.

Publisher's note Springer Nature remains neutral with regard to jurisdictional claims in published maps and institutional affiliations.



Open Access This article is licensed under a Creative Commons Attribution-NonCommercial-NoDerivatives 4.0 International License, which permits any non-commercial use, sharing, distribution and reproduction in any medium or format, as long as you give appropriate credit to the original author(s) and the source, provide a link to the Creative Commons licence, and indicate if you modified the licensed material. You do not have permission under this licence to share adapted material derived from this article or parts of it. The images or other third party material in this article are included in the article's Creative Commons licence, unless indicated otherwise in a credit line to the material. If material is not included in the article's Creative Commons licence and your intended use is not permitted by statutory regulation or exceeds the permitted use, you will need to obtain permission directly from the copyright holder. To view a copy of this licence, visit <http://creativecommons.org/licenses/by-nc-nd/4.0/>.

© The Author(s) 2025